Applications of Raman Spectroscopy and Chemometrics to Semiconductor Process Control

A thesis for the degree of

Master of Science

Submitted to

Dublin City University

By

Ian Robertson B.Sc.

Research Supervisor

Dr Enda McGlynn

School of Physical Sciences

Dublin City University

August 2000

Declaration

I hereby certify that this material, which I now submit for assessment on the program of study leading to the award of Master of Science is entirely my own work and has not been taken from the work of others save and to the extent that such work has been cited and acknowledged within the text of my work.

Signed: I. Robertson **ID No:** **97970301**

Ian Robertson

Date: 18/9/00

Table of Contents

Acknowledgements

I would like to thank my supervisor Dr Enda McGlynn for the opportunity to pursue research within this group. I thank Enda for his patience, encouragement and guidance throughout the course of this project. I would also like to thank Prof. Brian MacCraith for his help on different aspects of the research and the Chemistry department for their help at various stages.

I am grateful to my colleagues at DCU who made my time here very enjoyable and interesting, in particular Mark, Cathal, Jason, Clodagh, Eilish, Kieran, Pat and Roisin. A special thanks goes to the technical staff at the Physics department. Des and Al, I am very grateful. To Louise, thanks for the encouragement.

Finally, I would like to dedicate this thesis to my parents, George and Esther, for their unwavering support, understanding and patience.

Abstract

The Standard Clean (SC-1) solution, which contains a mixture of hydrogen peroxide (H_2O_2), ammonium hydroxide (NH_4OH) and water, makes up the most important part in the RCA cleaning process for semiconductor wafers. This step has proven to be the most effective method for the removal of contaminants.

The SC-1 solution is, however, very unstable due to the decomposition of H_2O_2 and the evaporation of NH_4OH. This work aims to use a combination of Raman spectroscopy and chemometrics in order to predict the concentrations of the individual components of unknown samples of SC-1. The attraction of such a technique is that it is non-invasive and therefore can be performed on-line. The potential cost-savings for semiconductor manufacturers are also considerable.

Both calibration and prediction sets were obtained for various concentrations of SC-1 solutions. The results of the analyses performed are presented here.

Chapter 1

Introduction

1.1 Introduction

The requirement for clean semiconductor wafers is becoming more and more important as semiconductor device geometries continue to shrink and die sizes grow. Such developments mean that microcontaminants such as particles and metallic impurities will have an ever-increasing detrimental impact on device yield and reliability.

Wet chemical processing has been widely used as a major cleaning tool in ultra large scale integration (ULSI) manufacturing and the current wet cleaning process for silicon wafers is based on the so called Radio Corporation of America (RCA) cleaning method introduced by Kern and Puotien in 1970.[1] One of the steps involved in the RCA process is the Standard Clean (SC-1), which contains a mixture of hydrogen peroxide (H_2O_2), ammonium hydroxide (NH_4OH), and water. This step has proven to be the most successful method for the removal of particles since it was first developed nearly thirty years ago, and has, therefore, become the most important cleaning technique in the manufacture of sub-micron devices.[2]

The SC-1 solution is, however, notoriously unstable due to H_2O_2 decomposition and evaporative losses of NH_3 and water.[3] The SC-1 composition shows considerable variation over time and is almost impossible to predict. Although in use for nearly thirty years little has been done in an attempt to control the chemical concentrations of the processing baths. Such concentration control is

essential for more uniform processing, chemical cost reduction, productivity enhancements, and for environmental reasons.

The purpose of this project was to develop a non-invasive technique for the prediction of the individual component concentrations of SC-1 using Raman spectroscopy in conjunction with chemometric techniques.

1.2 The Standard Clean (SC-1) Solution

The SC-1 solution consists of a mixture of ammonium-hydroxide, hydrogen-peroxide and water. The mixture has also been referred to as APM (Ammonium Hydroxide-Hydrogen Peroxide Mixture. This solution has been found to be the most efficient particle removal agent to date.[4] SC-1 solutions facilitate particle removal by etching the wafer underneath the particles; thereby loosening the particles, so that mechanical forces can readily remove the particles from the wafer surface. Megasonic energy can further aid particle removal through cavitation (bubble formation) and/or acoustic streaming (fluid motion).[5-7] The ammonium hydroxide in the solution steadily etches silicon dioxide at the boundary between the oxide and the aqueous solution (i.e., the wafer surface). The hydrogen peroxide in SC-1 serves to protect the surface from attack by OH^- by re-growing a protective oxide directly on the silicon surface (i.e., at the silicon/oxide interface). If sufficient hydrogen peroxide is not present in the solution, the silicon will be anisotropically etched and surface roughening quickly ensues. This surface roughening can adversely affect gate oxide breakdown. Conversely, hydrogen peroxide is known to readily dissociate and form water and oxygen. With such dissociation, bubbles can appear in the solution if the concentration of oxygen is too high. The gas-liquid interfaces that result from the formation of such bubbles can

then attract particles that may be in the liquid and can be re-deposited on the wafer if the bubbles come into contact with the wafer.[4]

The three components of SC-1 dissociate ionically as follows:

$$NH_4OH \leftrightarrow NH_4^+ + OH^- \quad (1.1)$$

$$H_2O_2 \leftrightarrow HO_2^- + H^+ \quad (1.2)$$

$$H_2O \leftrightarrow H^+ + OH^- \quad (1.3)$$

As a result of the above it is clear that the NH_4OH/H_2O_2 ratio is a very important parameter.[8-10] Kern and Puotien, developers of the solution in 1970, recommended a 1:1:5 weight/volume ratio, for $NH_4OH:H_2O_2:H_2O$ and this ratio has been adopted in most ULSI device production lines up to the present day. However recent studies in which the NH_4OH concentration in the SC-1 solution has been reduced to almost one-twentieth of the original concentration have shown a decrease in surface roughness on Si wafers and thus a reduction in device production costs due to this reduction in NH_4OH concentration.[11] Kaigawa *et. al.* claim that there is a possibility of oxide degradation in pre-oxidation wafer cleaning with SC-1 in which NH_4OH is present in a relatively high concentration. Si etching phenomena in SC-1 solution have been extensively investigated by many researchers.[12-15]

Maintaining the correct NH_4OH/H_2O_2 ratio remains a major problem however. SC-1 solutions are unstable due to the simultaneous loss of NH_3, H_2O_2, and H_2O. The loss of these components from SC-1 megasonic processing baths, especially ammonia and hydrogen peroxide, is dependent on upon a number of factors, which are difficult to predict and control. Hydrogen peroxide decomposition is concentration, pH and temperature dependent.[4] Moreover, homogeneous and heterogeneous catalysts play an important role in the

decomposition process. The decomposition process for H_2O_2 is given by the following reaction.

$$2H_2O_2 \leftrightarrow 2H_2O + O_2 \tag{1.4}$$

The influence that heavy metals such as iron can have in the decomposition of hydrogen peroxide has been documented previously.[16] Organic contamination in hydrogen peroxide may also play a role in its decomposition.

In the case of ammonia the loss mechanism is primarily by evaporation. The evaporation rate can be influenced by the strength of the exhaust over the bath, the bath operational temperature which is usually between 50° and 65°, and the amount of bath agitation which is induced by bath re-circulation. The possibility also exists that some loss of ammonia occurs by oxidation, which is expressed by the following half reaction.[4]

$$2NH_3 + 6OH^- \leftrightarrow N_2 + 6H_2O + 6e^- \tag{1.5}$$

1.3 SC-1 Compositional Analysis

Due to the importance of SC-1 process control, many techniques have been previously employed to analyse its composition with limited success. The two main fields of investigation have been in chemical analysis and spectroscopy. Conventional titration[17] and electrochemistry [4] have been the favoured chemical methods while UV absorption[18], near infra–red reflectance (NIR)[11] and to a lesser extent Raman scattering[19] have been are some of the spectroscopic techniques used to date.

While chemical analysis produces an extremely accurate indication of the concentration of each component within SC-1, its one major drawback is that it is an invasive technique and is, therefore, capable of introducing undesirable agents

which add to the complexity of the solution and also necessitate the need for frequent re-calibration. Furthermore, they are not well suited to on-line process control or any level of automation as frequently the process must be shut down in order to facilitate such measurements. Spectroscopic techniques can be applied non-invasively, but on the other hand, they have their limitations; an example being that UV absorption cannot detect NH_4OH.[20]

Mid-infrared spectroscopy, usually in the form of Fourier Transform Infrared (FTIR), is a widely used optical spectroscopic technique. Its advantages are that it produces data with good S/N consisting of sharp peaks that are readily identifiable with each chemical component. These peak areas can then be directly converted into numerical concentration values. However there are significant problems associated with the sampling process that restrict FTIR's usefulness in this application. These measurements require very short path lengths (10μm or less) and secondly the high absorbances can sometimes distort the linear relationship between the measured signal and the actual concentration.[20]

On the other hand, NIR (near infrared) spectroscopy can be used non-invasively; the NIR light being directed through a glass vial or cell, with either of the transmitted or reflected signals being recorded. However, the convoluted nature of the data returning requires that the instrument's software be calibrated on a large number of reference samples. Any minor change introduced in the process (particularly temperature) requires a complete re-calibration of the system. Also, both NIR and FTIR techniques can sometimes have difficulties with aqueous samples because of the strong water signals that are returned. Nevertheless there has been some success with NIR spectroscopy in Japan recently.[21]

1.4 Raman Spectroscopy and Chemometrics

The approach taken in this project was to use Raman spectroscopy coupled with chemometrics for the non-invasive quantitative analysis of SC-1. Raman spectroscopy has been shown to be excellent for the identification of atomic and molecular species. The use of Raman spectroscopy up until recently, however, was confined to research laboratories due to the need for high powered lasers with water cooled power supplies and the need for high performance double monochromators. When one considers such requirements coupled with a relatively weak Raman scattering signals from most samples it is possible to envisage why such a technique had found little usage within industry. However within the last decade a number of technologies have combined to ensure that Raman systems are now much more portable and compact than before. The advent of CCD detectors, compact solid state lasers, holographic filters and fibre optic laser light delivery have exposed Raman spectroscopy to a much broader base of applications, especially within the microelectronics, chemical, pharmaceutical, food and biomedical industries. Some other applications for Raman spectroscopy have been found in:

- the characterisation of diamond like carbon films[22]
- measurement of degree of polymerisation[23]
- pharmaceutical industry[24]
- silicon stress analysis[25]
- petroleum Analysis[26, 27]

Considering how much Raman technology has advanced in recent years it becomes clear why it is now an excellent process control technique, and is ideally suited to the current application. Also Raman spectroscopy gives very sharp well-defined

peaks in the SC-1 application. This is advantageous when analysing these spectra with both univariate and multivariate analysis techniques.

Chapter 2

Spectroscopic Methods and Sample Preparation

2.1 Introduction

The theory behind Raman Scattering is developed in this chapter. Although not a completely rigorous description, the fundamentals of both the classical and quantum mechanical formulations are discussed. Following this, an outline of the Kaiser Optical System's Holoprobe used in this project is given, and its specifications are described.

2.1.1 Raman Scattering

The Raman effect was first predicted by Smekal[28] in 1923 but it wasn't until 1928 that it was experimentally observed by Chandresekhara Venkata Raman, an Indian physicist[33] who was later awarded the Nobel Prize for his discovery.

Smekal predicted that radiation scattered from molecules not only contains photons with the incident photon frequency but also photons with a change in frequency. It is exactly this phenomenon that describes the Raman effect.

The Raman effect can be described as the inelastic scattering of light by matter. When a photon of light, too low in energy to excite an electronic transition from one state to another, strikes a molecule, it can be scattered in one of three different ways. Firstly the incident photon can be scattered elastically, i.e. the incident photon energy is the same as the scattered photon energy. This is also

known as Rayleigh scattering. The incident photon can also be inelastically scattered by either losing energy to, or removing energy from the molecule. The photon that loses energy to the molecule undergoes what is known as Stokes scattering and this excess energy within the molecule appears as vibrational energy in the form of a phonon,

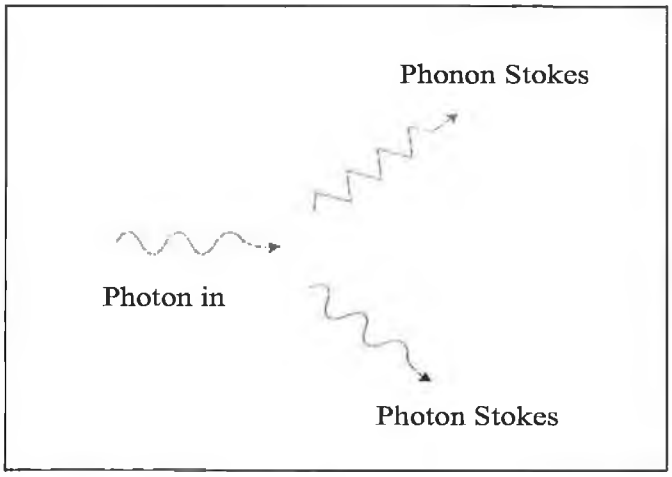

Fig 2-1: Stokes Scattering.

whereas the photon which gains energy from the molecule experiences anti-Stokes scattering, and the molecule loses vibrational energy in the form of a phonon. As indicated in Fig 2-2 the anti-Stokes process is dependent n the phonon population. It follows then that this process is temperature dependent as the phonon population increases with temperature.

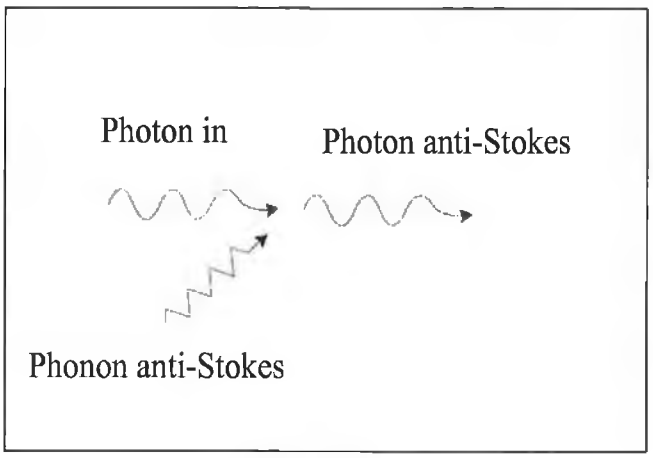

Fig 2-2: anti-Stokes scattering.

2.2 Classical Theory of Raman Scattering

The origin of Raman spectra can be explained by an elementary classical theory[29], i.e. the molecule as a collection of atoms undergoing simple harmonic vibrations with no quantisation of vibrational energy. Therefore the classical theory assumes that the molecule is a vibrating dipole. When a molecule is placed in an electric field a dipole moment is induced within the molecule due to the displacement of electrons relative to the nuclei. A fluctuating electric field will produce a fluctuating dipole moment of the same frequency. Such an electric field can be expressed as follows

$$E = E_0 \cos(2\pi\nu_0 t) \tag{2.1}$$

where E_0 is the intensity of the electric component, ν_0 is the wave frequency, and t is the time. For small fields the induced dipole moment μ_i is proportional to the field strength E.

$$\mu_i = \alpha E \tag{2.2}$$

Here α is the proportionality constant called the polarisability, which is a measure of the ease with which the electron cloud may be distorted by the presence of an external electric field. This induced dipole moment will emit or scatter radiation of frequency ν_0. This is Rayleigh scattering. Substituting 2.2 into 2.1 we obtain the equation determining the value of the dipole moment induced by the electromagnetic wave:

$$\mu_i = \alpha E_0 \cos(2\pi\nu_0 t) \tag{2.3}$$

If the molecule is vibrating with a frequency ν, the nuclear displacement is written as

$$q = q_0 \cos(2\pi\nu t) \tag{2.4}$$

where q_0 is the vibrational amplitude within the molecule. For small amplitudes of vibration, α is a linear function of q Therefore, we can write

$$\alpha = \alpha_0 + \left(\frac{\delta\alpha}{\delta q}\right)_0 q \tag{2.5}$$

Here α_0 is the polarisability at the equilibrium position and ($\delta\alpha/\delta q$) is the rate of change of α with respect to q in the course of a given vibration, characterised by the normal co-ordinate q, describing the displacement of all nuclei of the atoms in the molecule during vibration about their equilibrium positions. Now substituting Eqn 2.5 into Eqn 2.3 yields

$$\mu_i = \alpha_0 E_0 \cos(2\pi\nu_0 t) + \left(\frac{\delta\alpha}{\delta q}\right)_0 E_0 q_0 \cos(2\pi\nu t)\cos(2\pi\nu_0 t) \tag{2.6}$$

Eqn 2.6 can be rewritten as

$$\alpha_0 E_0 \cos(2\pi\nu_0 t) + \frac{1}{2}\left(\frac{\delta\alpha}{\delta q}\right)_0 q_0 E_0 \left\{\cos[2\pi(\nu_0 + \nu)t] + \cos[2\pi(\nu_0 - \nu)t]\right\} \tag{2.7}$$

The vibrating molecule can, therefore be a source of scattered radiation of three different frequencies: (i) of frequency ν_0 i.e. the frequency is unchanged with respect to the incident radiation, also termed Rayleigh scattering; (ii) of frequency (ν_0-ν), i.e. frequency equal to the difference of the frequency of the incident radiation and that of the vibrations of the molecule, known as Stokes scattering; and (iii) of frequency (ν_0+ν), i.e. the frequency equal to the sum of the frequencies of the incident radiation and the vibration of the molecule, known as anti-Stokes scattering. If $(\delta\alpha/\delta q)_0$ is zero the second term vanishes. Thus the vibration is not Raman active unless the polarisability changes during the vibration.

2.3 Quantum Theory of Raman Scattering

Electromagnetic radiation exhibits the properties of both a stream of particles and a wave. Therefore the Raman effect can be described in two ways. The previous interpretation is based on wave theory, which was the classic approach to electromagnetic radiation. However the quantum mechanical approach recognises the fact that the vibrational energy of a molecule is quantised showing particulate nature, and such particles are generally known as quanta. In the case of electromagnetic radiation they are also known as photons. The relationship between the energy E of a photon and its frequency is described by the Planck formula:

$$E = h\nu \tag{2.8}$$

The interaction of the photon with the molecule can yield three phenomena: absorption, emission and scattering. It is obviously scattering that interests us in the case of Raman spectroscopy. Scattering takes place within 10^{-14}s of when a photon, of energy not equal to the energy difference between any two stationary levels of the molecule, interacts with that molecule.

The normal Raman effect takes place when a photon, with an energy distinctly lower than that of the energy difference between the ground level and the first excited state, interacts with a molecule.

Scattering is a two-photon process[30, 31] that cannot be separated experimentally into two single photon steps of absorption and emission. The photon with an initial energy of $h\nu_0$ can (a) proceed without a change in energy (otherwise known as Rayleigh scattering), (b) experience a decrease in energy $h\nu_{R(St)}$(Stokes scattering), or (c) experience an increase in energy $h\nu_{R(aSt)}$ (anti-Stokes scattering). Fig 2-3 illustrates what happens when identical molecules are illuminated with monochromatic light.[33] The resulting spectrum is also shown.

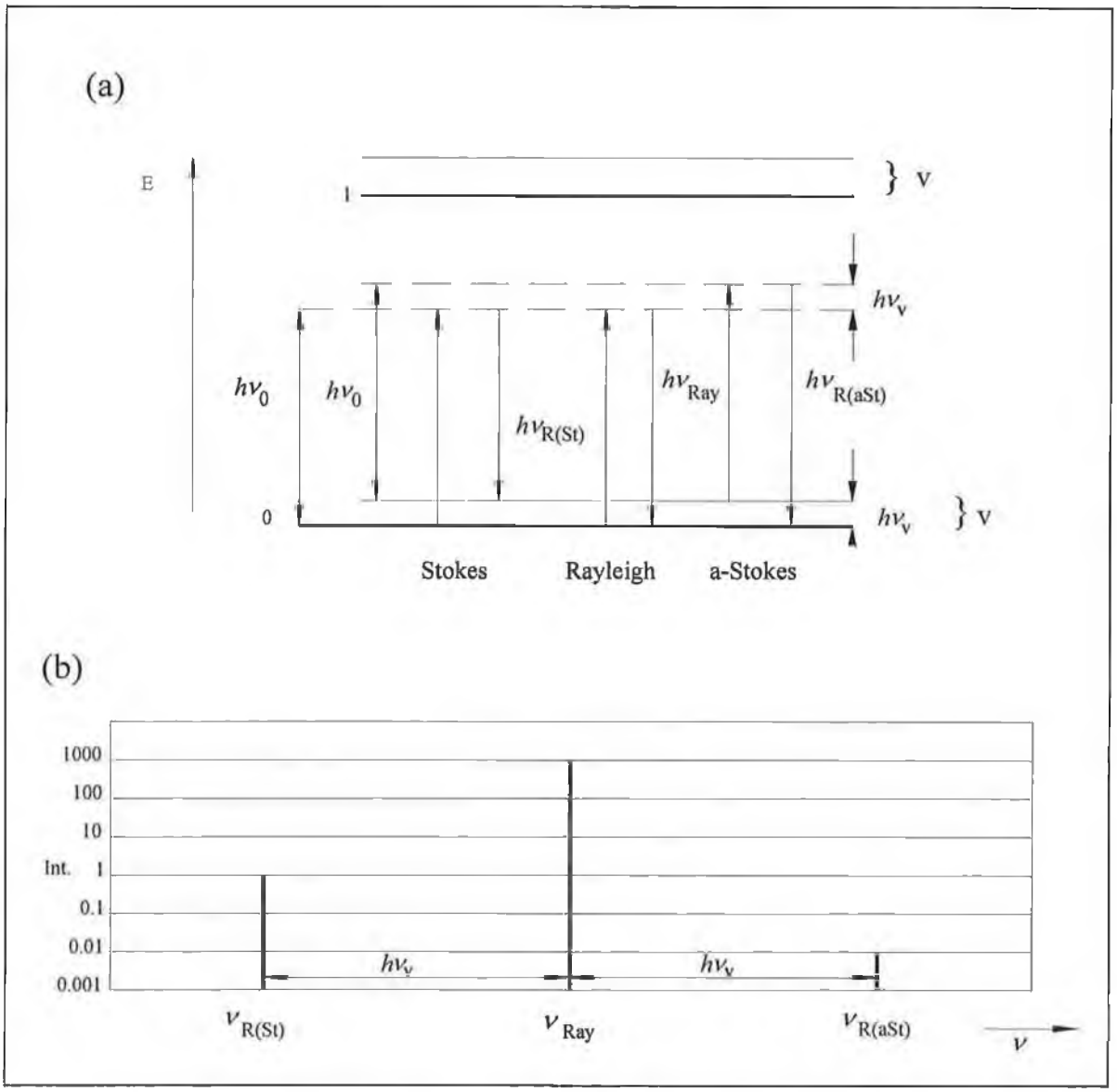

Fig 2-3: (a) Diagram of scattering during illumination with monochromatic light. (b) Part of the resulting spectrum, where ν_{Ray} is the Rayleigh Scatter, $\nu_{R(St)}$ is the Raman Stokes Scatter, $\nu_{R(aSt)}$ is the Raman anti-Stokes scatter, and ν_v is one of the possible vibrational frequencies of the molecule.

Two electronic levels are shown. Ground state level (0) and the first excited state (1). The vibrational levels are also illustrated. The dashed lines depict two virtual levels of the molecule, separated by $h\nu_v$ where ν_v is one of the possible vibrations of the molecule. According to the Boltzmann law, most of the molecules will occupy the vibrational ground state at room temperature. This is why Stokes

transitions are more likely to occur than anti-Stokes transitions. When the molecules are irradiated with photons of energy $h\nu_0$ we observe a spectrum, Fig 2-3(b). The strong line in the centre is the Rayleigh line. This frequency ν_{Ray} is equal to that of the incident light and is typically 10^3-10^4 times stronger than that of the Raman frequencies $\nu_{R(St)}$ and $\nu_{R(aSt)}$. This means that the Rayleigh signal must be effectively filtered out so that the Raman signal isn't swamped (see section 2.4.1.2). Also luminescence signals can easily swamp the Raman signal. The absolute differences between the frequencies of the incident photon and both scattered photons are the same as the molecular vibration frequency.

$$h\nu_0 - h\nu_{R(St)} = h\nu_v \quad \text{and hence} \quad \nu_0 - \nu_{R(St)} = \nu_v \tag{2.9}$$

$$h\nu_{R(aSt)} - h\nu_0 = h\nu_v \quad \text{and hence} \quad \nu_{R(aSt)} - \nu_0 = \nu_v \tag{2.10}$$

From the above, it is possible to see how the difference in frequency between the incident photon and the scattered photon is characteristic of a molecule and independent of the frequency of the incident radiation. It is important to note that Raman scattering is governed by selection rules determined by the symmetry and electronic structure of the system, and such considerations are an important factor in Raman studies of materials, particularly crystalline solid state materials. In the case of liquid samples however, where the molecular orientation is random, such considerations are less important, and have not been considered in any detail in this work.

2.4 Kaiser Holoprobe Integrated Fibre Coupled Raman System

The various parts that make up the Kaiser Holoprobe Raman system used in this project are outlined below.

2.4.1 System Overview

Shown below in Fig 2-4 is an outline of the Kaiser Optical Holoprobe Raman system. Holographic optics, the probe head and the CCD camera are of particular interest in terms of the modern Raman instrument. These allow for much quicker Raman data collection.

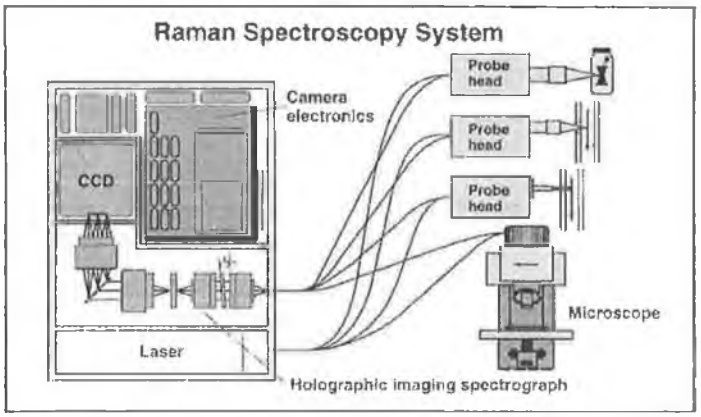

Fig 2-4: Outline of Kaiser Raman system

2.4.2 Holographic Optics

The Kaiser Holoprobe embraces all the recent technologies that make up the modern Raman instrument. The emergence of holographic optics has been central to the development of portable Raman systems. The Holoprobe uses volume phase holograms for both filtering and dispersion functions. The advantages of such holograms are manifold. They provide a combination of high efficiency, low scattering and controllable spectral response.[34] Volume phase holograms are periodic refractive index gradients generated in transparent materials. Such periodicity means that these holograms diffract light. The thickness of the

holograms can vary from ~3μm to 100μm and they operate in the Bragg (volume) diffraction regime. The most common example of Bragg diffraction is X-ray diffraction. In the Bragg regime, diffraction occurs through an angle, θ, given by Eqn 2.11 and illustrated in Fig 2-5,

$$\theta = \sin^{-1}\left(\frac{m\lambda}{2d}\right) \tag{2.11}$$

In Eqn 2.11 m is the order of diffraction, λ is the wavelength and d is the fringe spacing. For a sufficiently thick grating, diffraction is efficient in only the +1 and 0 orders.

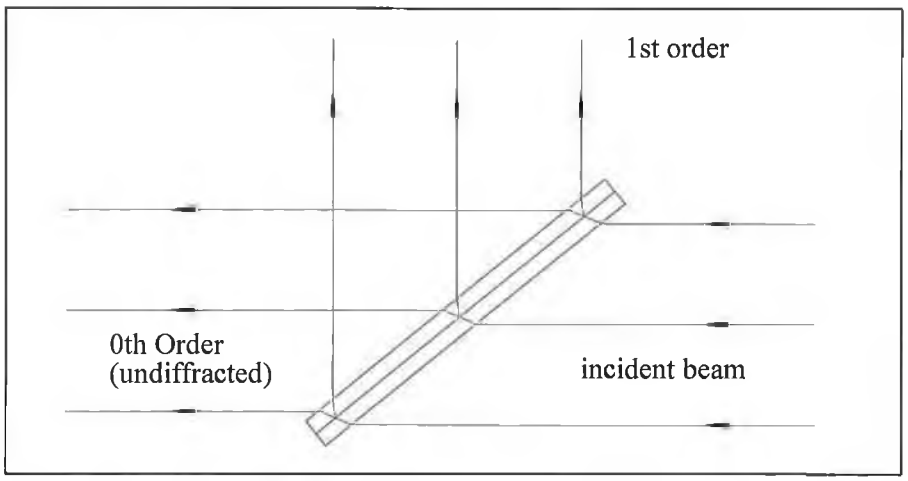

Fig 2-5: Simple illustration of Bragg diffraction using tilted grating, 0^{th} order undiffracted.

2.4.2.1 Holographic Gratings

In order to obtain a large spectral bandwidth, holographic gratings use thin films, which can result in light being diffracted into orders other than +1 and 0. The grating used in the Kaiser Holoprobe exhibits diffraction in one order only and therefore no light is lost to other, evanescent orders. Overall, a volume transmission holographic grating can have a diffraction efficiency of 80% or greater for unpolarised light. It is also possible to stack transmission gratings one after another

in order to extend their operating range. The Kaiser HoloPlex grating is constructed in this manner as shown in Fig 2-6. The two gratings are stacked consecutively in such a way that hologram A would cover 0-2000cm^{-1}, for example, and hologram B 2000-4000cm^{-1}. The two regions then viewed by the CCD are then 'stitched' together to give the spectrum as we see it. This allows for wider wavelength-region coverage (without a loss in resolution) than would be available with a single grating.

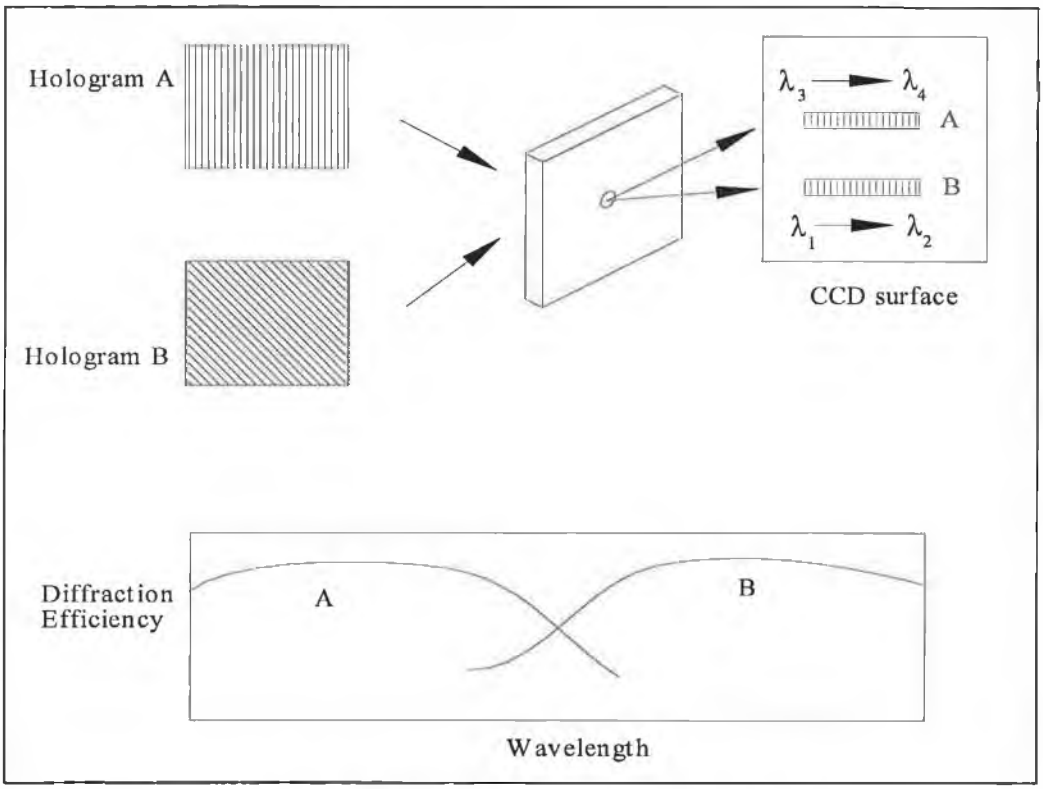

Fig 2-6: The construction of a holographic grating

2.4.2.2 Holographic Filters

The planes of equal refractive index of a volume-holographic diffraction grating are perpendicular to the surface of the hologram or are tilted at a slight angle. If the fringes are parallel to the surface of the grating the hologram acts as a wavelength selective mirror, more commonly called a notch filter. Thus, it rejects a narrow band of wavelengths and transmits all others. The reflectivity of a notch

filter can be quite high and its bandwidth narrow. This makes notch filters ideal laser light rejection filters for work in Raman spectroscopy. The greatest advantage of a holographic notch filter is the smoothness of its transmission curve, which means it performs much better at low wavenumbers than a thin dielectric filter. Undulations in a dielectric filter's transmission curve means that the measurement of vibrational frequencies below 400-500cm^{-1} becomes nearly impossible. Also, the holographic filter has a narrower rejection band that further enhances its low frequency performance advantage.

2.4.2.3 The Axial Transmission Spectrograph

The axial transmissive spectrograph for the Holoprobe uses a holographic transmission grating in combination with well corrected camera lenses to achieve peak performance. The diffracted light from the spectrograph stage is focused onto the surface of a CCD detector, which records the actual spectrum. The light path is axially symmetric through the input and output lenses which minimises aberrations in the system. The grating is at an angle close to 45° so that the diffracted light is forced into the +1 order for highest diffraction efficiency. The complete spectrograph is shown overleaf in Fig. 2-7. The first lens collimates the input signal from the slit, which then passes through the notch filter to attenuate the laser light. The filtered signal is incident on the grating and focused onto the CCD by the second lens. The slit also functions as a resolution spatial filter to minimise the transmission of stray light into the dispersion stage of the spectrograph.

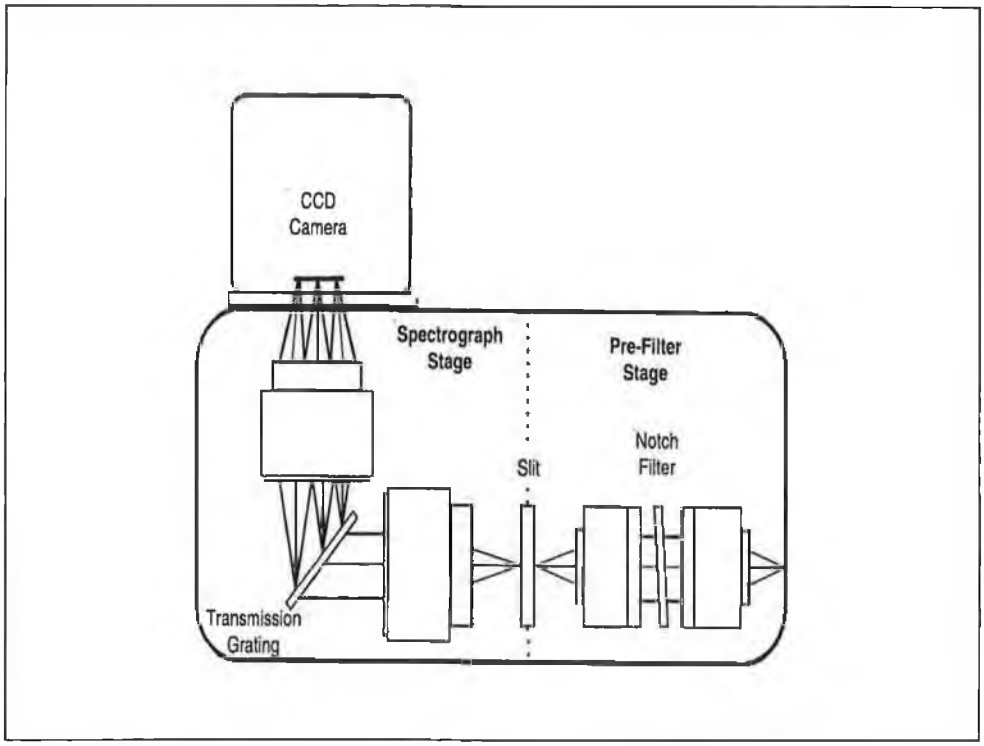

Fig 2-7: Outline of Axial Transmission Spectrograph showing location of pre-filter stage, slit, lenses, grating and camera.

2.4.3 Helium Neon Laser

The light source used with this particular model of Holoprobe is a 20mW He-Ne laser, operating at a wavelength of 632.8nm.

2.4.4 CCD Camera

The array detector used in the Raman Holoprobe is a charge coupled device (CCD) detector. The popularity of CCDs arises out of the fact that they combine low noise, large dynamic range, and high quantum efficiency with the ability to store and measure charge in two dimensions thus having the capacity to represent images. A CCD can be viewed as a two dimensional array of potential wells or metal oxide semiconductor (MOS) capacitors, each of which is an individual pixel.

The number of electrons collected in a well is directly proportional to the number of photons incident on that pixel. The best signal to noise ratio is obtained when the exposure of the CCD detector allows the wells to nearly fill. The most significant source of noise in most CCDs is quantum or `shot' noise. Shot noise arises from the random arrival times and energies of incident photons. Two consecutive spectral measurements of the same sample will always show some variation in the number of photons collected at any pixel. Longer collection times can reduce the relative levels of shot noise.

Dark current and cosmic rays can also contribute to the production of inaccurate spectra. Dark current is a background external current that is produced even when there is no radiation incident on the detector and leads to a dark current curve. Cosmic rays are high-energy particles, originating from space that lead to spikes in the spectra. The contributions from both dark current and cosmic rays can be corrected for within the software package.

2.4.5 Fibre Optic Probe

Multimode optical fibres are an excellent choice for laser light delivery and collection. They are small, can be used for remote or laboratory sampling and provide stable reproducible signals from solids, liquids and gases. However silica optical fibres themselves are a source of considerable background signal. As the laser light is travelling down a length of fibre, it generates an intense silica Raman spectrum. Fluorescence from the fibre cladding and from the cement holding the bundle together is also generated. These signals emerge from the fibre head along with the laser light. They are then reflected from any solid or liquid and collected with the Raman spectrum of the sample. This reflected laser light generates more

background as it returns down the fibre and these signals can obscure weak Raman signals. The fibre optic probe in the Holoprobe, shown in Fig. 2-8 eliminates this problem by using a lens to both filter the laser light before fibre delivery onto the sample and to collimate the Raman scattered light. Also the collected light is focused onto a single fibre.

The light emerging from the fibre is collimated by lens assembly PL-1 and passes through a holographic transmission grating, G in Fig. 2-8, which diffracts the laser light towards a spatial filter (PL2 and PL3). The laser is then focused on the sample. Only the laser wavelength passes through this spatial filter as all the silica Raman light is removed at this stage. The collected Raman scatter, along with the Rayleigh scatter and reflected laser radiation, is passed through a pair of notch filters. These filters remove reflected laser light and any fibre background generated as the Raman signal travels to the spectrograph. The use of microscope objective lenses, PL4, allows efficient delivery and collection with single fibres. The Raman signal is then focused onto the fibre by PL5

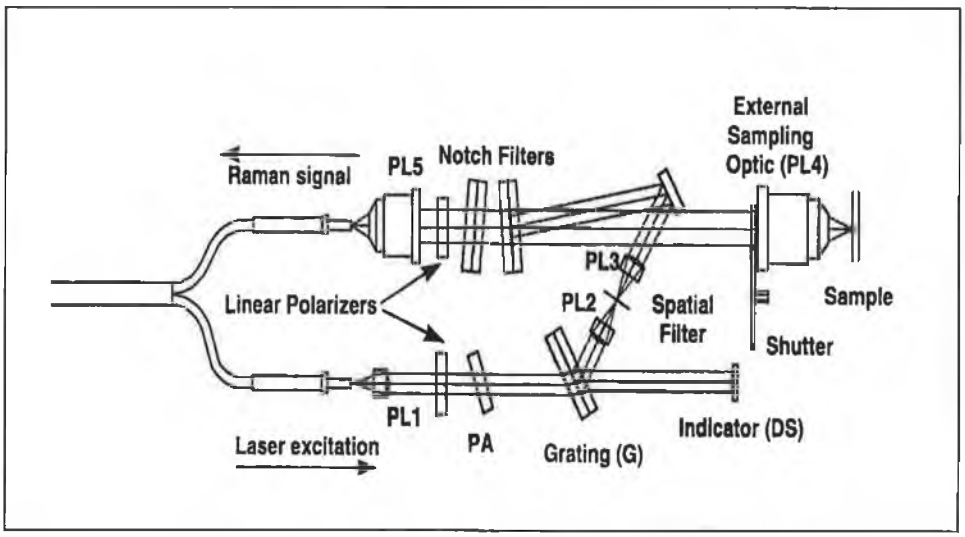

Fig 2-8: Diagram of fibre optic probe-head design showing lenses one through five (PL1-PL5), power adjustment control (PA), grating (G), diffuse screen indicator (DS), probe head shutter, spatial filter (SF), beam combiner and notch filters, and the linear polarisers (PB).

2.5 Sample Preparation

The *de facto* industry standard ratio for the ammonium/peroxide mixture (APM) is a 1:1:5 ratio of H_2O_2:NH_4OH:H_2O. Therefore the samples used in this study were made up in this way. Some results were also obtained for 1:1:4 and 1:1:6 ratios as well. For the 1:1:5 mix, 300ml of de-ionised water was used. Without dilution the NH_4OH and H_2O_2 were described as being 100% solutions for this particular example. The NH_4OH and H_2O_2 were kept at a constant volume of 50ml. The ammonia and peroxide were ratioed inversely in such a way that their sum total equalled 100%. For example, if there was 30ml of peroxide, this meant that 20ml of ammonia was present, i.e. 60% peroxide and 40% ammonia. To obtain these percentages the peroxide and ammonia were diluted. Therefore a 50 % ammonia solution was obtained by adding 25ml of water to 25ml of ammonia. Spectra were taken at 5% increments, as detailed overleaf.

Samples were prepared as required. For each change in percentage peroxide and ammonia, new solutions were made up. The SC-1 was not allowed to stand for any time and spectra were taken almost immediately. Also for each percentage data point, three batches of that concentration were prepared and analysed.

% Peroxide	% Ammonia	ml Peroxide	ml Ammonia	ml Water
0	100	0.0	50.0	300
5	95	2.5	47.5	300
10	90	5.0	45.0	300
15	85	7.5	42.5	300
20	80	10.0	40.0	300
25	75	12.5	37.5	300

30	70	15.0	35.0	300
35	65	17.5	32.5	300
40	60	20.0	30.0	300
45	55	22.5	27.5	300
50	50	25.0	25.0	300
55	45	27.5	22.5	300
60	40	30.0	20.0	300
65	35	32.5	17.5	300
70	30	35.0	15.0	300
75	25	37.5	12.5	300
80	20	40.0	10.0	300
85	15	42.5	7.5	300
90	10	45.0	5.0	300
95	5	47.5	2.5	300
100	0	50.0	0	300

Table 2.1 Solution Make-up.

2.6 Titrations

To further analyse the samples, titrations were performed on separate samples in order to determine the exact concentrations of peroxide and ammonia within the solutions, i.e. the number of moles in each sample.

2.6.1 Hydrogen Peroxide

Potassium permanganate is a powerful oxidising agent and can be used to estimate the end-point of titrations involving reducing agents such as H_2O_2. 5ml samples of SC-1 were taken and the appropriate amount of sulphuric acid added in order to facilitate the reaction. No indicator is needed for permanganate titrations.

$$5H_2O_2 + 2KMnO_4 + 3H_2SO_4 \rightarrow K_2SO_4 + 2MnSO_4 + 8H_2O + 5O_2 \qquad (2.12)$$

2.6.2 Ammonium Hydroxide

The first approach to titrating the ammonia was to employ a back titration method using sulphuric acid (H_2SO_4) and sodium hydroxide (NaOH). 5ml samples of SC-1 were taken from the batch solution and excess sulphuric acid was added to this. The sulphuric acid served to neutralise any ammonia in the solution and the excess was then titrated with NaOH using a phenolphthalein indicator. By calculating how much excess H_2SO_4 was present and how much there was initially, it was possible to determine how much was used up neutralising the ammonia. Hence the ammonia concentration was calculated. The reaction processes are outlined below.

$$2NH_4OH + H_2SO_4 \rightarrow (NH_4)_2SO_4 + 2H_2O \qquad (2.13)$$

$$2NaOH + H_2SO_4 \rightarrow Na_2SO_4 + 2H_2O \qquad (2.14)$$

This titration method proved unreliable over time, possibly due to the fact that NaOH is not a primary standard[1]. NaOH absorbs CO_2 from the atmosphere every time it is left exposed. This was replaced by sodium carbonate (Na_2CO_3) which is a primary standard and the H_2SO_4 was replaced by HCl simply because it reacts in a 1:1 ratio with NH_4OH. The appropriate reactions are:

[1] A primary standard is a substance that is easy to obtain, purify, dry and preserve in a pure state

$$NH_4OH + HCl \rightarrow NH_4Cl + H_2O \quad (2.15)$$

$$Na_2CO_3 + 2HCl \rightarrow 2NaCl + H_2O + CO_2 \quad (2.16)$$

2.7 Sample Holder

A sample holder was made in order to ensure consistent sample-probe separation. This is beneficial in that it helps reduce baseline fluctuations from sample to sample. Fig 2-9 shows a diagrammatic sketch of the holder.

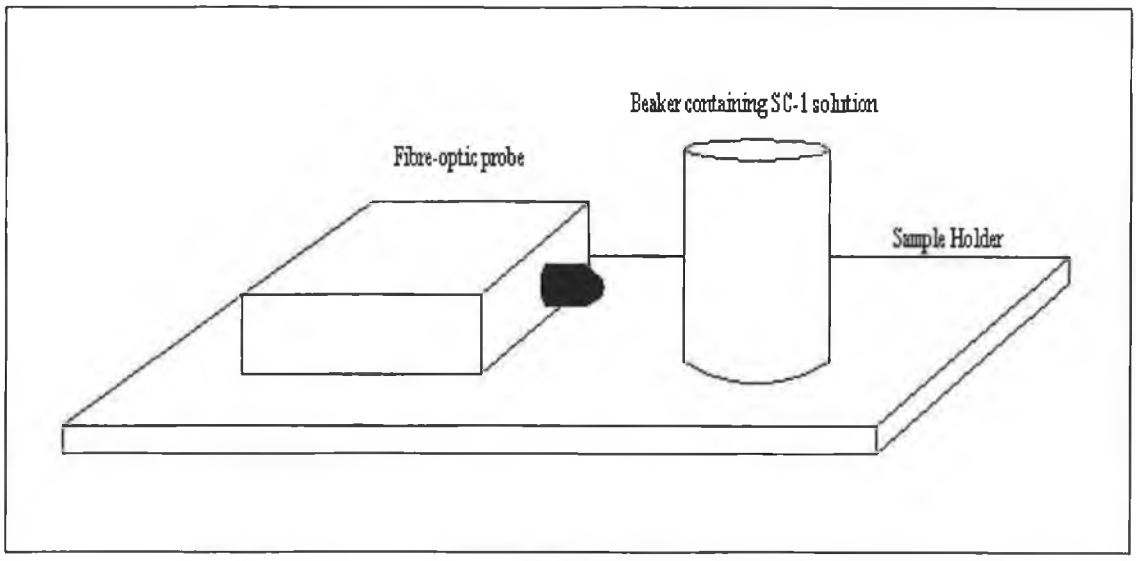

Fig 2-9: Diagram of sample holder containing beaker and fibre-optic probe.

2.8 System Set-up

Three spectra were taken for each sample each of 5 seconds duration and 5 accumulations. The cosmic ray filter was switched on and the dark current subtracted. All of this was done within the Holograms package. These spectra were then averaged for each sample and the three samples for each percentage were also

averaged to one. The spectra were then exported to the chemometrics software package, Unscrambler 7.01, where all of the analyses were performed

Chapter 3

Chemometrics

3.1 Introduction

Multivariate analysis, or chemometrics as it is widely known, has been defined as the chemical discipline that uses mathematical, statistical and other methods employing formal logic to (a) design or select optimal measurement procedures and experiments, and (b) provide maximum relevant chemical information by analysing chemical data.[35] The advantage of multivariate techniques as opposed to, say, the univariate approach is that by taking into account every, or at least a large number of variables from a spectrum, it is possible to gauge the influence of each particular data point on a model. This contrasts with the univariate approach where discarding potentially valuable information is possible. Multivariate calibration, then, means determining how to use many measured variables $x_1, x_2, \ldots\ldots\ldots x_n$ simultaneously for quantifying some target variable y.[36] In this work the Raman signal at various wavelengths and the concentration of the peroxide/ammonia are the x and y variables respectively.

3.2 Univariate Analysis

Univariate analysis is best described as simple linear regression, i.e. where there is one y variable being predicted from a second one, x, e.g. the intensity at a single wavelength and the relationship between the two is linear. In other words all observations are dependent upon a single variable x.

3.2.1 Least Squares Regression

Least-Squares regression is used to describe the relationship between y and x in general. The following method is as outlined in the work of Tedesco *et al.*[34] This relationship can be defined by the function $y=f(x,a,b_1.....,b_m)$ where $a,b_1.....b_m$ are constant coefficients characteristic of the regression line, representing the intercept of the line with the y-axis and the gradient of the line, respectively. The x value is the controlled or independent variable whereas the y value is the dependent or measured variable. This means that there is assumed to be no error in the x variable. However, on the condition that the error in preparing the samples is significantly smaller than the measurement error, which is usually the case, then this is a safe assumption for calibration problems. The values of a and b must be chosen so as to best fit the experimental data (x_i, y_i). If the relationship between x and y is considered to be a straight line then the relationship between each observation pair (x_i, y_i) can be described as

$$\hat{y}_i = a + bx_i \tag{3.1}$$

with the values of $\hat{y}$ being the estimated, model values. The generally accepted requirements for deriving the best straight line between $\hat{x}$ and $\hat{y}$ is that the difference between the measured and fitted line is minimised. The most popular technique to minimise this error is the least squares method. For each measured value the deviation between the derived model value and the measured data is given by $\hat{y}_i - y_i$. The total error between the model and the observed data is the sum of these individual errors. Each error is squared to make each value positive. Therefore, the total error, ε, is

$$\varepsilon = \sum_{i=1}^{n} (\hat{y} - y_i)^2 \tag{3.2}$$

which is the sum of the squared deviations. The minimum error can be found using partial differential calculus. From Eqns 3.1 and 3.2 we can substitute our model equation into our error definition

$$\varepsilon = \sum_{i=1}^{n} (a + bx_i - y_i)^2 \tag{3.3}$$

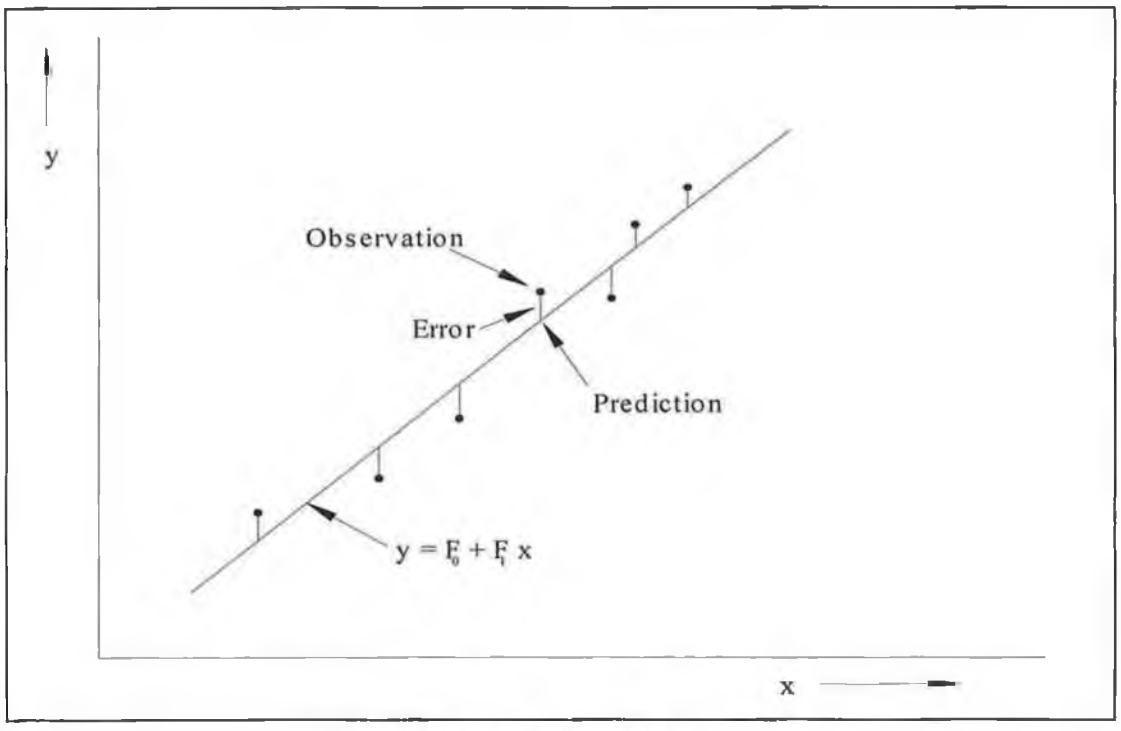

Fig 3-1: Least Squares Fit.

The values for a and b are independent unknowns which can be determined by differentiating with respect to a and b, respectively, and setting the results equal to zero,

$$\frac{\delta \varepsilon}{\delta a} = \sum_{i=1}^{n} 2\left(\hat{a} + \hat{b}x_i - y_i\right) = 0 \tag{3.4}$$

$$\frac{\delta \varepsilon}{\delta b} = \sum_{i=1}^{n} 2x_i\left(\hat{a} + \hat{b}x_i - y_i\right) = 0 \tag{3.5}$$

where $\hat{a}$ and $\hat{b}$ are least squares estimates of the intercept, a and slope, b.

Expanding and rearranging Eqns 3.4 and 3.5 gives two simultaneous equations

$$n\hat{a} + \hat{b}\sum x_i = \sum y_i \tag{3.6}$$

$$\hat{a}\sum x_i + \hat{b}\sum x_i^2 = \sum (y_i x_i) \tag{3.7}$$

from which the following expressions can be derived,

$$\hat{a} = \bar{y} - \hat{b}\bar{x} \tag{3.8}$$

and

$$\hat{b} = \frac{\sum (x_i - \bar{x})(y_i - \bar{y})}{\sum (x_i - \bar{x})^2} \tag{3.9}$$

where $\bar{x}$ and $\bar{y}$ represent the mean values of x and y.

3.3 Multivariate Analysis: An Example

Univariate analysis is limited to modelling a dependent variable with a single independent variable. However chemometrics is more often concerned with multivariate measurements. Therefore it is important to extend our understanding of regression to include cases in which several independent variables contribute to the measured response.[34]

Measuring the moisture content in flour using NIR[37] (near infrared reflectance) illustrates the power of multivariate analysis. The moisture content of flour has a strong absorbance peak at 1940nm. This peak is removed when the sample is dried as can be seen in Fig 3-2.

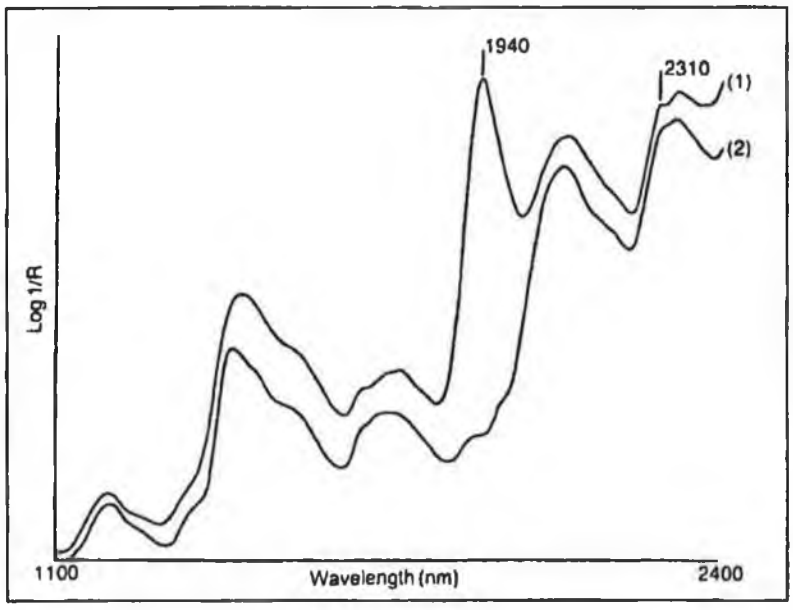

Fig 3-2: NIR spectra of flour sample (1) before drying and (2) after drying.

However, if for example, samples are taken and the reflectance measured at 1940nm, no correlation can be found between the moisture content and the absorbance as can be seen in Fig 3-3.

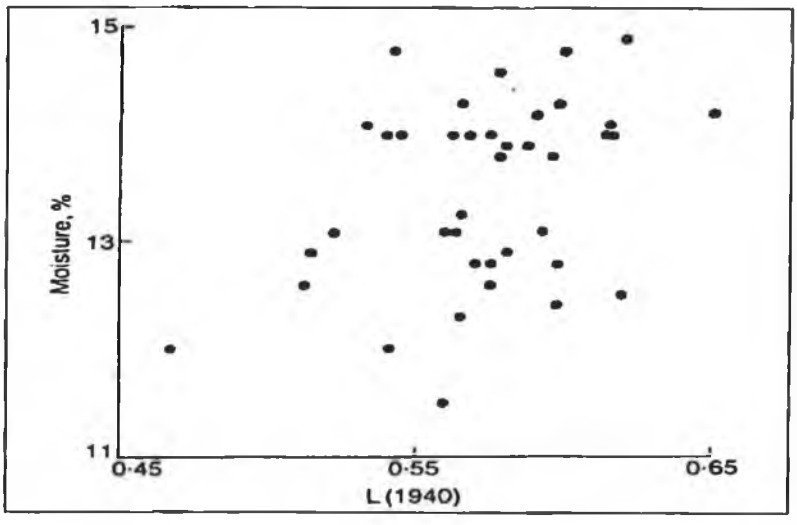

Figure 3-3: Moisture content versus log 1/R at 1940 nm for 40 samples of flour.

This is due to the fact that particle size affects the spectrum at all wavelengths, as depicted in Fig 3-4.

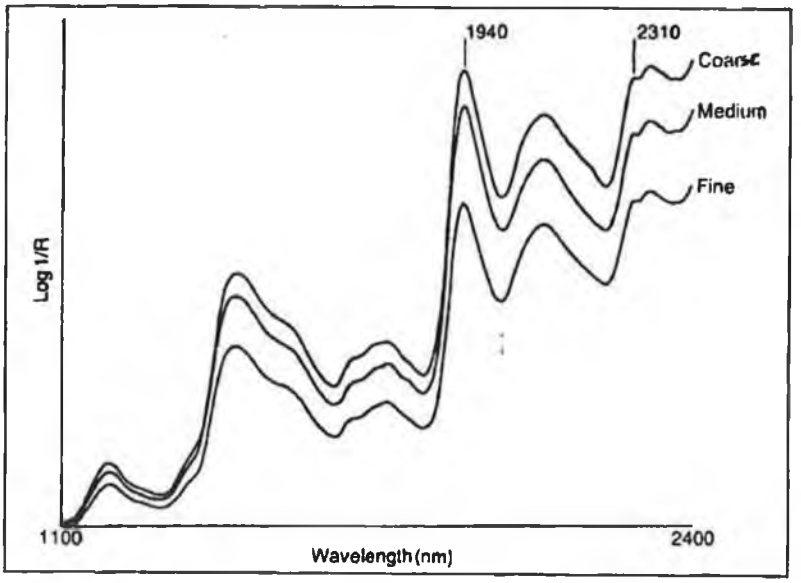

Figure 3-4: NIR spectra of three flour samples with the same composition but ground to three different particle sizes.

One solution is to normalise the reflectance at 1940nm with respect to a reference wavelength of 2310nm, in this case, to correct for particle size variations. This works well as illustrated below in Fig 3-5, where a good linear relationship is evident.

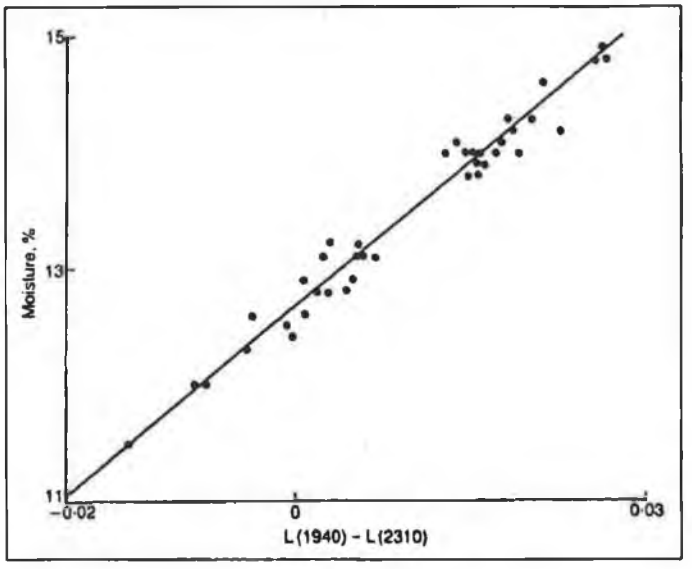

Fig 3-5: Moisture content versus ΔOD = log (1/R) at 1940nm – log (1/R) at 2130nm for 40 samples of flour.

The preceding example perfectly illustrates the need in some cases for multiple wavelength selection.

3.3.1 Introduction to Multivariate Analysis

In its simplest form, the dependent response variable, y, may be a function of two such independent variables, x_1 and x_2.

$$y = a + b_1 x_1 + b_2 x_2 \tag{3.10}$$

Here a is the intercept on the ordinate y-axis, and b_1 and b_2 are the partial regression coefficients. These coefficients denote the rate of change of the mean of y as a function of x_1, with x_2 constant, and the rate of change of y as a function of x_2 with x_1 constant respectively. The statistical technique most commonly used to derive a and b_1.....b_m is Multiple Linear Regression (MLR). It is however becoming popular to use Principal Components Regression (PCR) and Partial Least Squares Regression (PLS). The methodology used here to derive an understanding of these techniques is a rather intuitive one. Details of the precise algorithms for principal components analysis and partial least squares regression may be found in the appendices. Two concepts needed in order to understand these techniques are (a) fitting a line by least squares, which was dealt with in the previous section and (b) the projection of a multi-dimensional cloud of data points onto a line, which can be visualised quite easily. By combining these two techniques it is possible to gain an insight into MLR, PCR and PLS.[37]

From the method of least squares we have the equation $y = a+b_1x$. If a and b are found from the plot by measuring the intercept (a) and the slope (b_1), y can be predicted from x using the equation and the plot can be discarded. It is common, however that more than one x is needed for predicting y, i.e. in the case of

overlapping peaks. This means that we have at least two spectral measurements or two x's, x_1 and x_2. By ignoring y, temporarily, x_2 can be plotted against x_1 for the calibration samples as in Fig 3-6(a) below. The data are displayed as a point cloud in two dimensions. With one x only one dimension is needed to represent the point cloud as in Fig 3-6(b). If we had data as in Fig 3-6(b) it would be possible to find an equation using least squares.

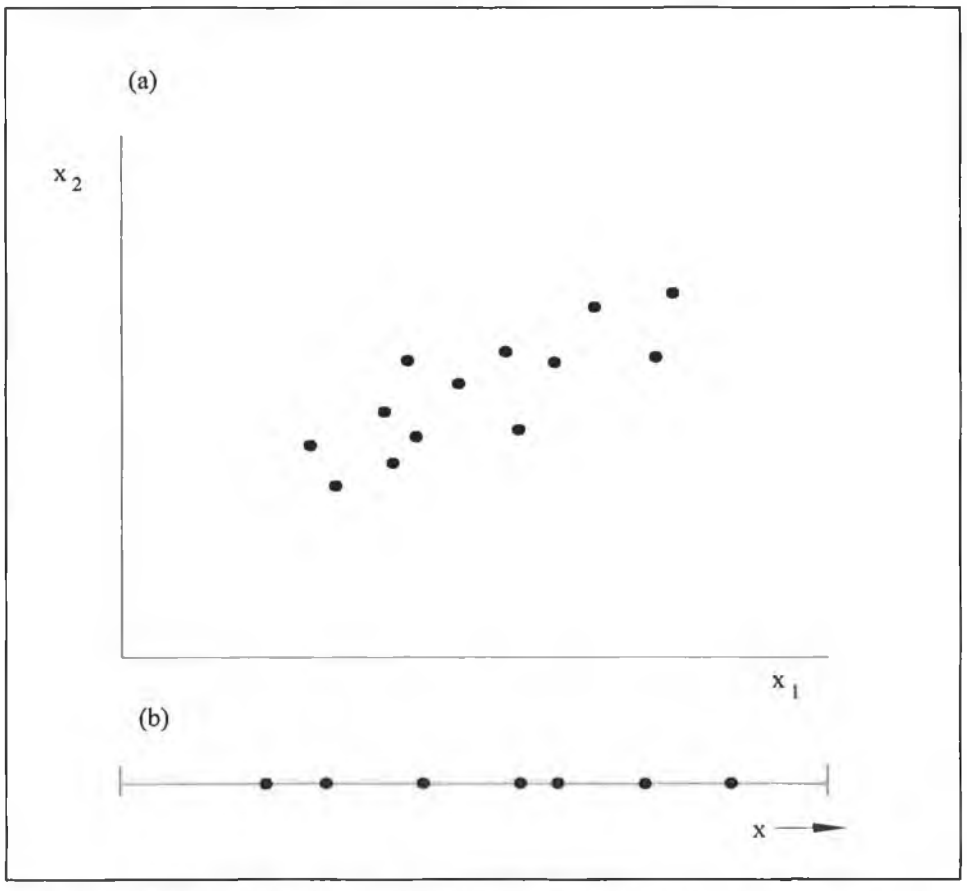

Fig 3-6: Point clouds in (a) two dimensions and (b) projected onto one dimension.

For more than one x it is necessary to reduce a multi-dimensional point cloud to one dimension as shown in Fig 3-7. A straight line is drawn and all the points are projected onto that line. From each point in two-dimensional space we find the nearest part of the line and project the point there. This projection has in turn created a new variable z.

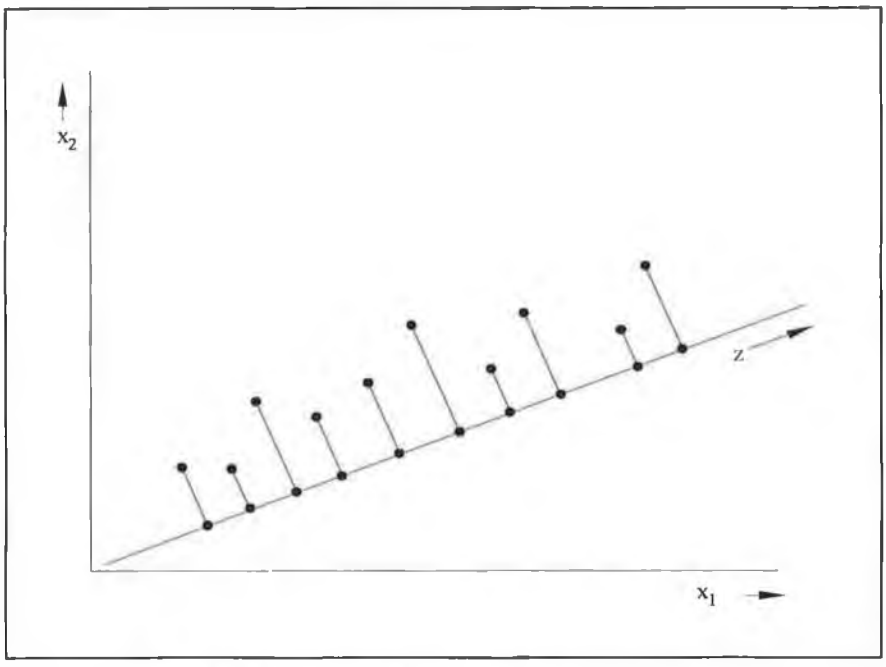

Fig 3-7: A projection from two dimensions to one.

The value of z for each sample can be found by measuring the distance from the origin to that point on the line. z can also be determined from the equation $z=c_1x_1+c_2x_2$ where the c's are constants that depend on the direction of the line. Having combined the two x's into one z it is now possible to plot y against z and to use least squares approach to find a prediction equation $y=a+b_1z$. By using the relationship between z and the x's this equation can be written as.

$$y = a + (b_1c_1)x_1 + (b_1c_2)x_2 \tag{3.11}$$

Now we have a two variable equation in the original x's. This is, essentially, the way in which all multivariate regression techniques operate. The remaining problem is the choice between the seemingly limitless possible projections, each of which gives a different z and hence a different prediction equation. MLR, PCR and PLS each has their own way of choosing their best projection and the way in which each does defines that particular technique. MLR chooses the z that gives the smallest value of R (the total squared prediction error) when fitted to the y's by least

squares. PCR and PLS in their simplest form operate in the same way as MLR, i.e. create a z by projection and predict y from z by least squares.

PCR chooses its projection without looking at the y's. It chooses so that z has as much variability as possible in order to create the best one-dimensional picture of the original x's. PLS combines both methods by choosing a projection that balances the variability of z and the error in predicting the known y's. In other words, it maximises the variability of z times the squared correlation of the y-z equation. Clearly the mathematics generalises to more variables as can be seen from the algorithms in appendices A and B, and in practice, formulae are used to find a and b directly. However this intuitive method, as described in the Near Infra-Red Publications (NIRP) chemometrics training course[37], gives an excellent insight into the principles of multivariate regression.

3.3.2 Principal Components Analysis

To gain further insight into multivariate analysis it is useful to examine Principal components Analysis (PCA) in more detail. PCA forms the basis for the regression techniques used in this work and also it provides an excellent foundation for the understanding of PLS and PCR.

PCA is a data compression technique that can reduce a large number of variables into small number of new uncorrected variables, which retain most of the information of the original set. [38] PCA is widely applicable to e.g. interpreting the chemical influence of specific components without prior knowledge of the chemical composition of the samples. It can also be used for identifying the influence of instrumentation on the data collected and how this can be used to improve instrument design.

3.3.2.1 Geometric Interpretation of Principal Components Analysis

PCA can be interpreted in terms of a 3-D data cloud. Although the number of dimensions in reality is much higher it gives a useful insight into the workings of PCA. The first step is to centre the data. This moves the origin from the bottom left corner to the centre of our space. The principal components are the new axes on which we will plot the data. The derivation of principal components (PC) are governed by the following rules:

- All PC's must pass through the origin
- PC's are orthogonal variables, i.e. they lie at right angles to each other
- PC's are derived in fixed sequence, with each PC representing less variation than the previous PC.

The first PC is the line, passing through the origin, which represents the maximum variation in the data. This maximum variation can be determined by least squares

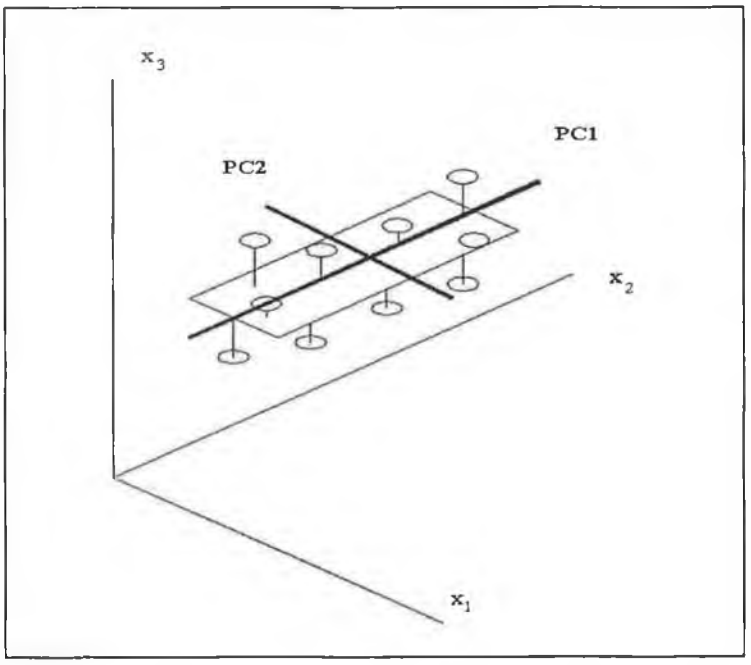

Fig 3-8:Projection of data cloud onto its principal components.

Two variables that define the first PC can be calculated now that its position is fixed. PC loadings are the rotations required to move the original axes to the position of the new PC. They are in fact the cosines of the angles between the new and each original variable.

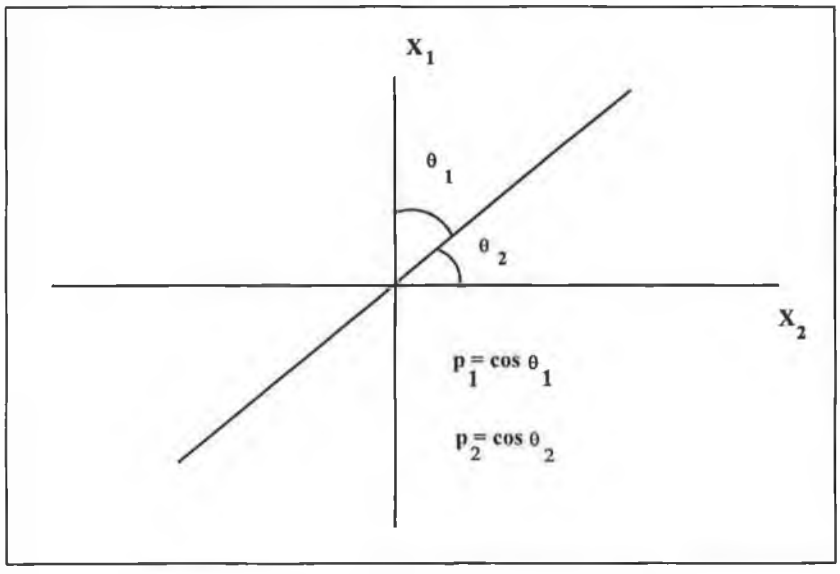

Fig 3-9: Determination of PC loadings.

PC scores are the response of each sample on each PC. They are the distances from the origin to the projection of each point at right angles to the PC.

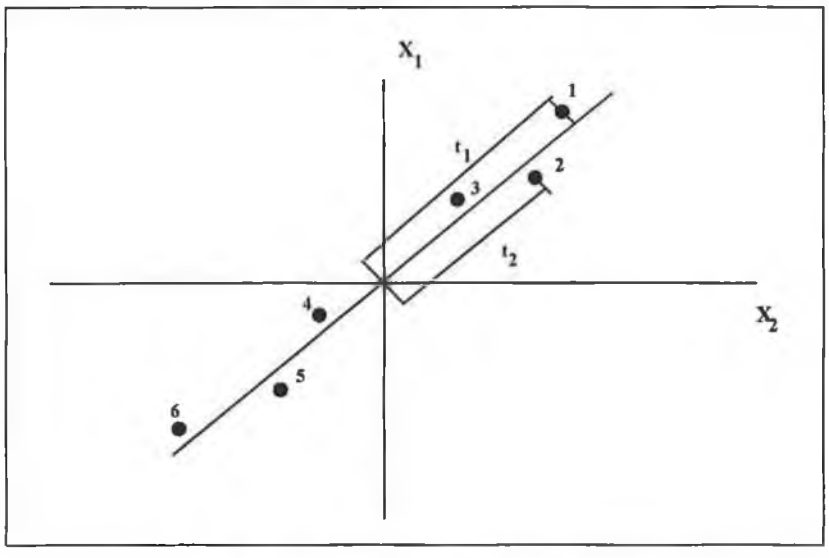

Fig 3-10: Determination of PC scores.

Chapter 4

Data Analysis

4.1 Introduction

The data collection and analysis was carried out in a stepwise fashion in which there were three main procedures.

1. Firstly, a simple univariate analysis was carried out in order to establish the basis for the technique, i.e. an experimental set of data to prove that the hydrogen peroxide and ammonium hydroxide peaks vary linearly with concentration.

2. Secondly, a multivariate calibration and validation were carried out, of which there were two parts. A simple percentage method was first performed to prove the efficacy of the multivariate approach, followed by a more absolute determination of concentrations, the results of which were verified by titrations.

3. Finally, a second multivariate calibration and validation was performed in an attempt to further improve the accuracy of predictions and thus reduce the error.

4.1.1 Raman Spectrum of SC-1 Solution

Illustrated below in Fig 4-1 is the Raman spectrum of the industry standard SC-1 cleaning solution (1:1:5 volume ratio of 35% (w/v) H_2O_2 : 35% (w/v) NH_4OH : H_2O). This is a typical SC-1 Raman spectrum and all the major detail is visible. The strong band centred near 3450cm^{-1} is from the –OH stretching vibration of water. The weaker band at 1630cm^{-1} is the water bending mode. The sharp band at 3315cm^{-1} is from the –NH stretch of NH_4OH. This band was used for the quantitative determination of NH_4OH. The sharp band at 875cm^{-1} is from the H_2O_2 O-O stretching vibration. The 875cm^{-1} feature was used previously for the quantitative determination of H_2O_2.[3]

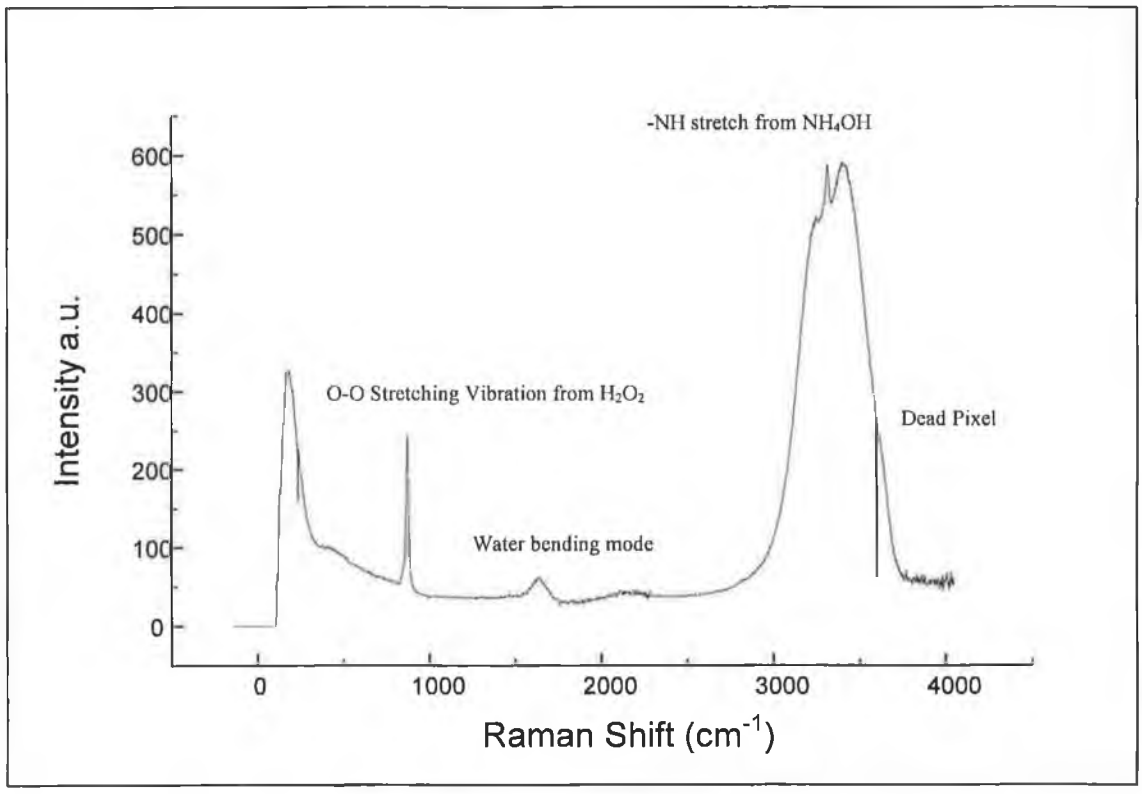

Fig 4-1 Raman Spectrum of SC-1 solution showing the O-O stretching vibration from H_2O_2 at 875cm^{-1}, the –NH stretch from NH_4OH at 3315cm^{-1} and the water bending mode centred at 1630 cm^{-1}.

4.2 Univariate Analysis of Raman Spectra

The univariate approach to calibration takes into account only one dependent variable and in the case of the SC-1 solution this is the area under the hydrogen peroxide peak at ~875cm^{-1} and the ammonium hydroxide peak at 3315cm^{-1}. These areas were then plotted against the particular concentration in order to build a calibration curve. This was a preliminary step in order to determine whether or not the reagents' peak areas would vary linearly with a change in concentration. As can be seen from Fig 4-2 and Fig 4-3 they clearly do. In the case of the H_2O_2 peak the concentration varied from 5% in 5% increments to 25% H_2O_2. For the NH_4OH the concentration varied from 25% in 5% decrements to 5% NH_4OH. Three spectra were taken at each concentration. A baseline was set and the area under each curve was measured. These areas were averaged and then plotted against concentration as illustrated in Figs. 4-2 and 4-3 below.

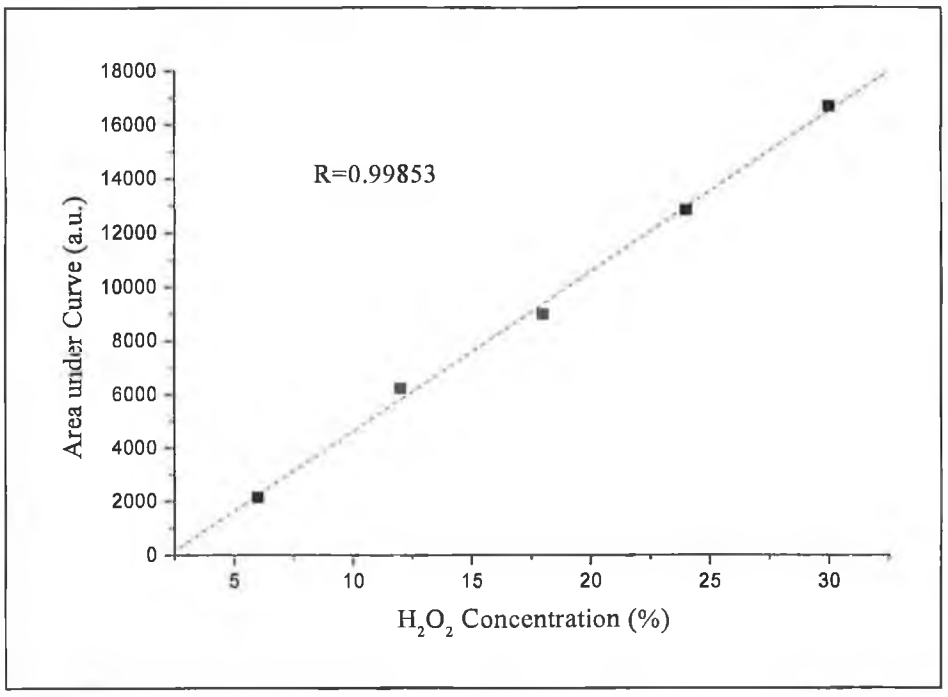

Fig 4-2: Graph of H_2O_2 peak area @ 875cm^{-1} versus % H_2O_2.

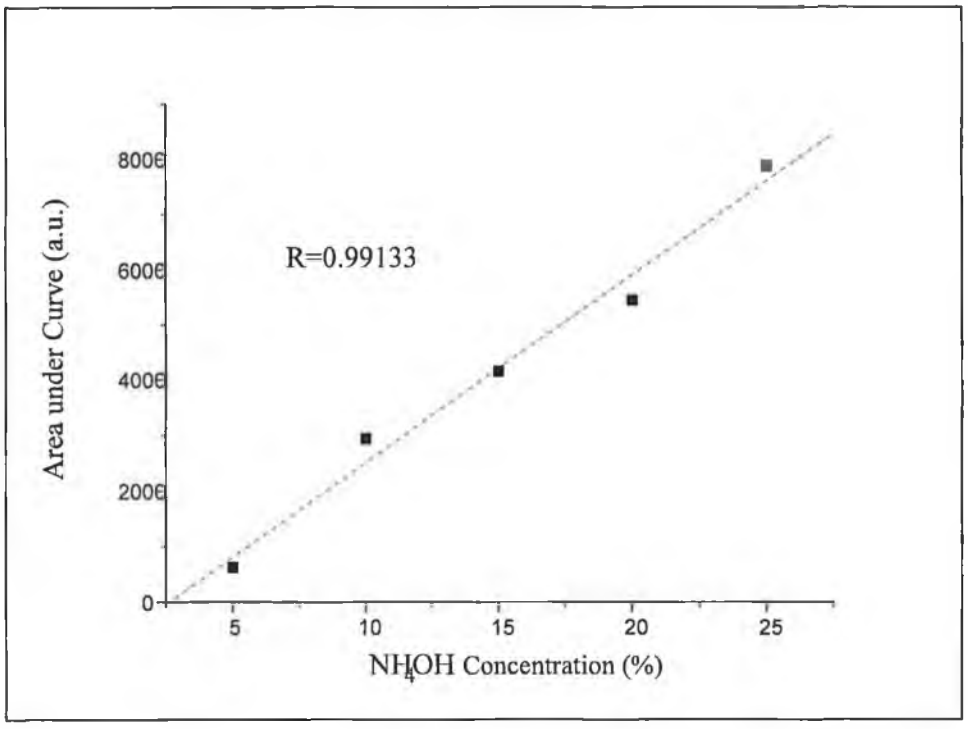

Fig 4-3: Graph of NH_4OH peak area @ 3315cm^{-1} versus % NH_4OH.

The above calibration curves show the linear variation of the Raman signal with concentration. These were not used for prediction purposes but for proof of principle.

4.3 Multivariate Analysis

For the multivariate section two main calibration sets were obtained, the details of which are outlined below. Before considering the calibration sets it is informative to view the regression coefficients for both peroxide and ammonia models. These identify the pertinent peaks within a specific calibration.

4.3.1 Regression Coefficients

Figs. 4-4 and 4-5 are the regression coefficients for the individual models that were built, i.e. for the peroxide model and the ammonia model. Regression coefficients indicate the influence of each data point on that particular model. In the

case of Fig 4-4 it is clear that in the case of an increase in concentration of H_2O_2 the changes in the spectrum are centred on the 875cm^{-1} peroxide peak. An illustration of regression coefficients can be useful for analysis of spectra that contain many peaks and it isn't clear exactly which peaks are affecting the model. It allows for the identification of the pertinent peaks. When the ammonia model was built it can be seen that the 3315cm^{-1} peak has most influence on the model, as expected

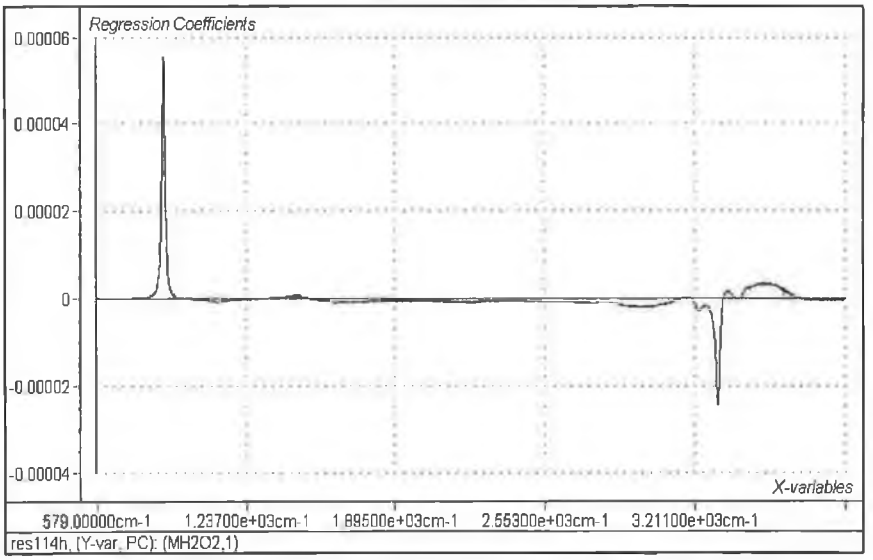

Fig 4-4: Regression coefficients for Hydrogen Peroxide model.

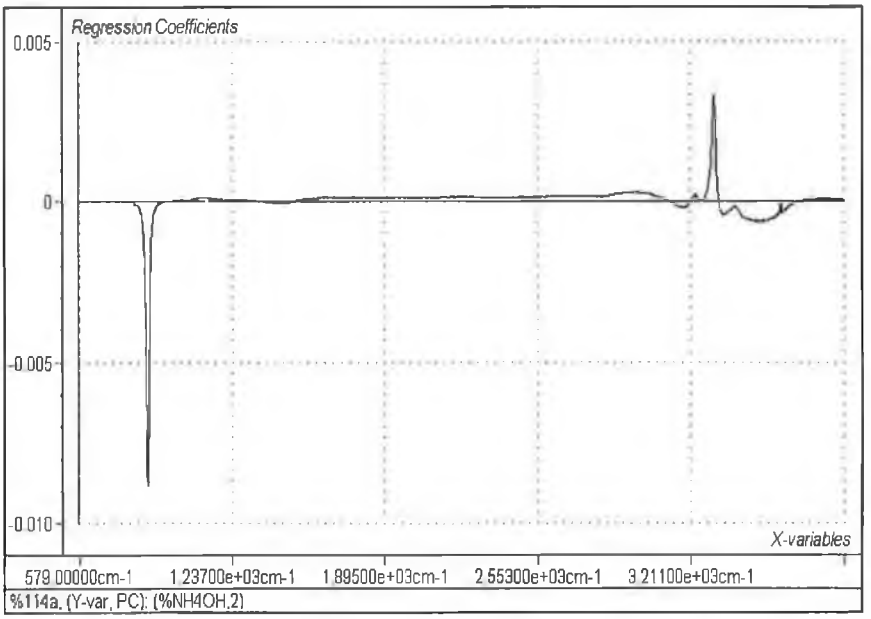

Fig 4-5: Regression coefficients for Ammonium Hydroxide model.

4.3.2 Calibration 1

The primary aim within this calibration set was to acquire a two-dimensional calibration model by not only varying the H_2O_2/NH_4OH ratio but also by changing the water ratio. Therefore three sets were measured starting at a 1:1:4 ratio of H_2O_2 : NH_4OH : H_2O and working up to a 1:1:6 ratio. Within each of these sets the H_2O_2/NH_4OH ratio was varied from 0% H_2O_2/100% NH_4OH in 5% increments/decrements to 100% H_2O_2/0% NH_4OH. Three samples were made up for each step and three spectra were recorded for each sample. To obtain an absolute measurement three 5mL samples were titrated to obtain the number of moles of both peroxide and ammonia as outlined in section 4.2. Therefore both percentage and molar calibration sets were obtained for each ratio.

4.3.2.1 Percentage Models, Hydrogen Peroxide

Shown below in Fig 4-6 is the scores plot for the 1:1:5 percentage models for both peroxide and ammonia. As illustrated in Chapter 3, scores are the response of each sample on each principal component (PC). Therefore, it is useful to look at the scores plot for the detection of outliers. For each model built the accompanying scores plot is shown.

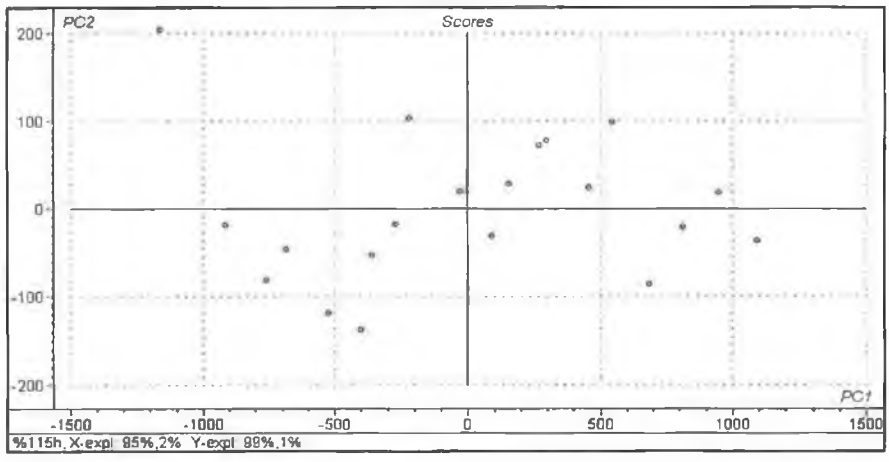

Fig 4-6: Scores plot for H_2O_2 'percentage' model.

Fig. 4-7 is a predicted versus measured plot for the model. This plot indicates the 'goodness of fit' of the model. A defining standard is the Root Mean Square Error of Prediction (RMSEP). This gives an indication of the errors involved in the model. The advantage of RMSEP is that it gives errors in the units that are used in the model, percentage or number of moles. The method of validation employed is Full Cross Validation (FCV). This works in the following way. Firstly the model is built using partial least squares (PLS). Then each data point is taken out of the model and the model tries to predict for this data point. The difference between the predicted value and the calibration value is called the Standard Error of Prediction (SEP). When the SEP is found for each data point it is then possible to find the RMSEP. The RMSEP is the average of all the SEP's and can be can be seen on each Predicted versus Measured graph. However the RMSEP cannot be solely relied upon when evaluating a model. To build a robust model an independent test set should be predicted and the errors examined in this case. This is *the* 'litmus' test for a good model.

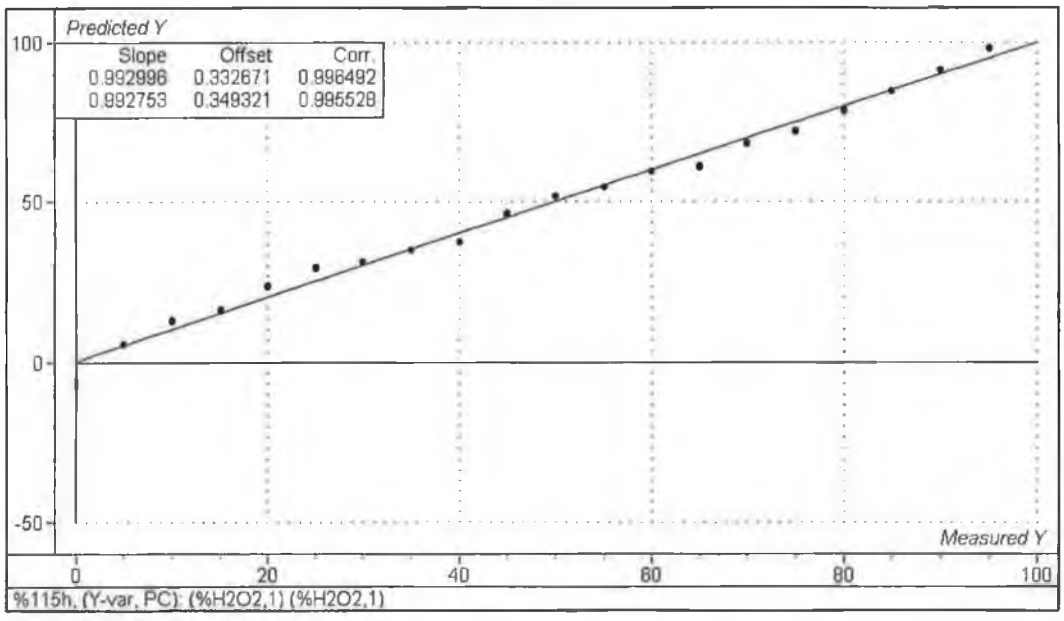

Fig 4-7: Predicted versus Measured plot for H_2O_2 'percentage' model.

Table 4-1 summarises both the calibration and prediction results for this particular model, which is a percentage calibration for H_2O_2. Test sets were examined in the 50%-100% range. It is not practical to test in the lower regions as SC-1 baths will never deteriorate to that level. This range, 0-100% was used in calibration to provide more data points. Furthermore, at lower percentages and molar concentrations, percentage errors become inordinately large.

% H_2O_2	Calibration	Validation	Test-Set	Deviation	RMSEP = 2.72
50	51.65	51.73	48.94	1.06	
60	59.67	59.63	62.38	2.38	
70	68.52	68.33	71.19	1.19	
80	78.84	78.60	77.56	2.46	
90	91.04	91.17	88.39	1.61	
95	97.56	98.04	96.85	1.85	

Table 4-1: Calibration and Prediction data summary for H_2O_2 'percentage' model.

As can be seen from the above table the results returned were quite satisfactory. The calibration values can be thought of as how well the algorithm relates the changes in the ascribed concentration values to the changes in the spectra. The calibration values compare very favourably with the exact values. The validation method used in all of the models built is Full Cross Validation (FCV). The RMSEP can be thought of as the average prediction error for each validation point. In this model this value is excellent at <2.72% which points to the fact the model may be useful for prediction purposes. Yet it is only when a test-set is used that the true value of the model can be estimated. The test-set prediction values prove very favourable with deviations of <3%, which for the purposes of this project are excellent and compare very well with similar industrially aimed systems where deviations of 3% are common.[22]

4.3.2.2 Ammonium Hydroxide

The NH_4OH was calibrated in the same way as H_2O_2. A scores and predicted versus measured plot are shown followed by a summary of results.

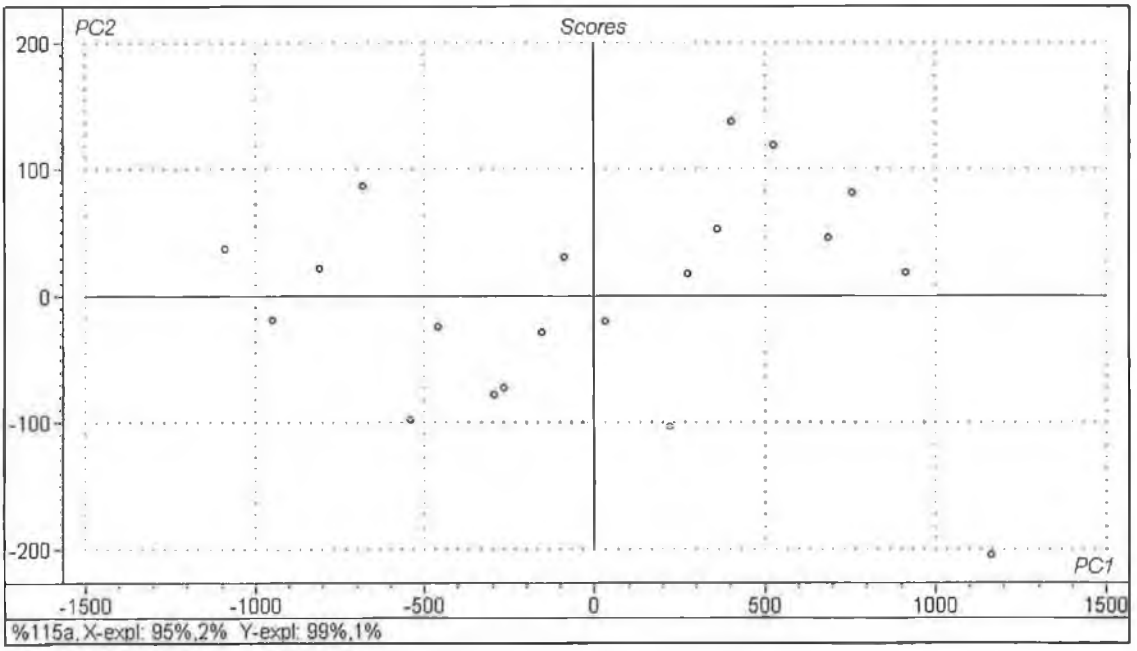

Fig 4-8: Scores plot for NH_4OH 'percentage' model.

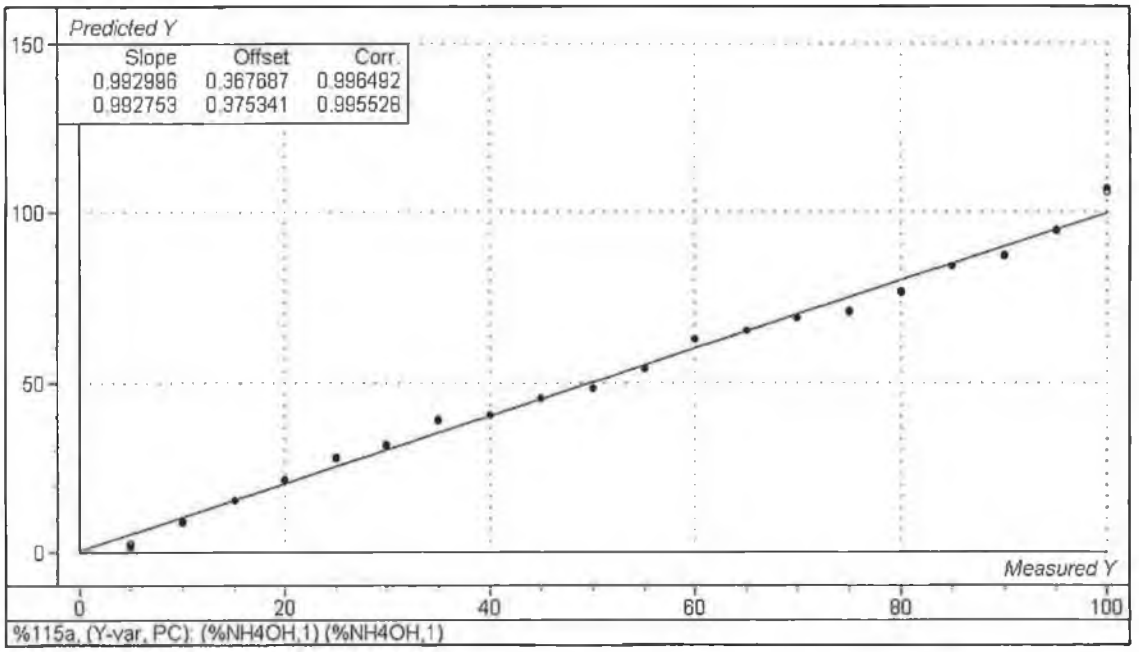

Fig 4-9: Predicted versus Measured Plot for NH_4OH 'percentage' model.

% NH_4OH	Calibration	Validation	Test-Set	Deviation	RMSEP = 2.72
50	48.34	48.27	52.19	2.19	
60	62.62	62.74	57.71	2.29	
70	68.99	68.90	69.11	0.89	
80	76.68	76.28	77.39	2.61	
90	87.32	86.88	88.64	1.36	
95	94.51	94.31	93.77	1.23	

Table 4-2: Calibration and prediction data summary for NH_4OH 'percentage model.

The NH_4OH results are again good as can be seen from Figs. 4-8 and 4-9 and Table 4-2 although not as accurate as the peroxide results. This can be attributed to the fact that NH_4OH is an extremely volatile substance and also its 3315cm^{-1} band sits on top of a water band, which means it is harder to interpret than the peroxide band which stands alone. The calibration and validation values are good within an error range of <4%. The RMSEP is low also, standing at 2.72%. Therefore, when re-entered into the model as a validation point each of the calibration points returned an error value of, on average, 2.72%. The test-set also proves reliable with deviations all within the RMSEP value. This means that the model, like the peroxide one is robust and capable of predicting unknown concentrations of NH_4OH reliably.

4.3.2.3 Molar Models, Hydrogen Peroxide

The second method used was a model to predict absolute concentrations, i.e. the number of moles of peroxide or ammonia present, for both calibration and prediction purposes. This meant that it was possible to independently verify the predicted values that were based on absolute concentrations within the calibration set. However, absolute prediction and comparisons have historically proven difficult due to human error and the large influence that baseline variations have on such models.

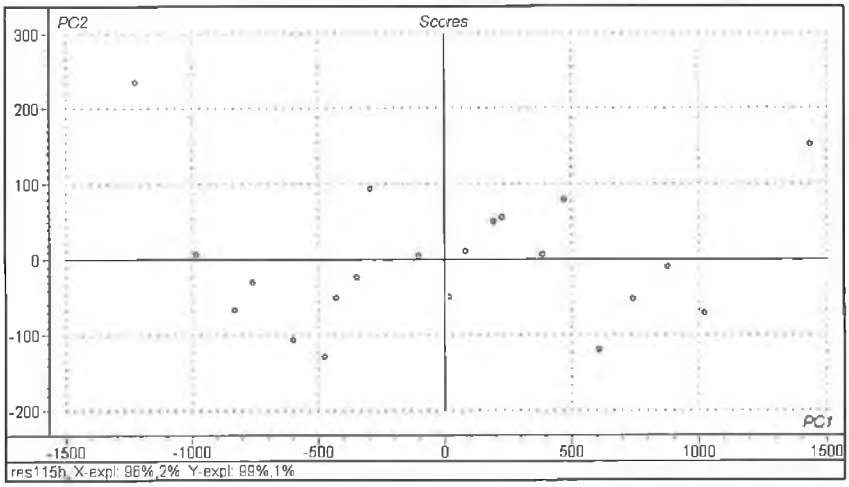

Fig 4-10: Scores plot for H_2O_2 molar model.

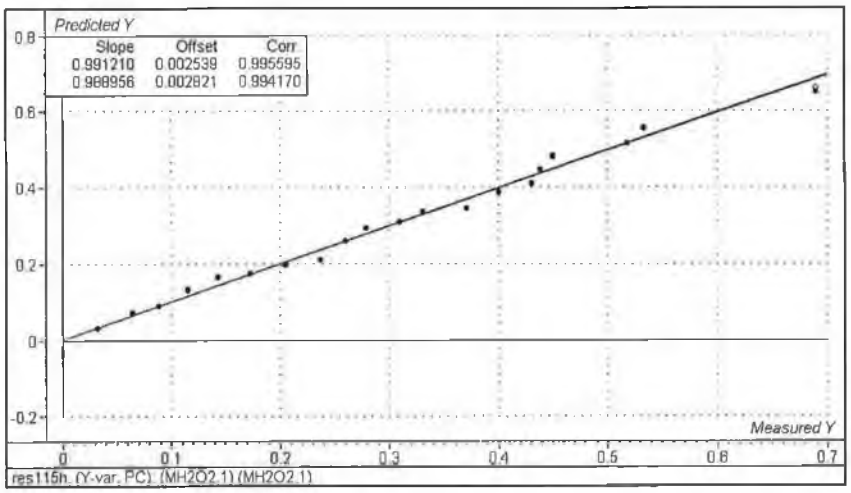

Fig 4-11: Predicted versus Measured plot for H_2O_2 molar model .

H_2O_2 (mol)	Calibration	Validation	Test-Set	Predicted	Deviation	RMSEP = 0.019
0.278	0.293	0.294	0.283	0.301	0.018	
0.330	0.339	0.339	0.321	0.343	0.022	
0.400	0.389	0.388	0.415	0.395	0.020	
0.439	0.447	0.447	0.456	0.458	0.022	
0.518	0.517	0.517	0.532	0.501	0.031	
0.689	0.661	0.648	0.697	0.668	0.029	

Table 4-3: Calibration and prediction data summary for H_2O_2 molar model.

The values for the peroxide molar model prove to be quite good and the test-set reliable too. As can be seen from the above Table 4-3 the calibration and validation values are very close to the titrated values and the RMSEP is low also, especially

when it is compared to the solutions of higher concentrations. The test-set proves the reliability of the model as both predicted and titrated values for the same solution are very much in accordance with each other. The deviations are low percentage-wise with all of them being within ~7% error range.

4.3.2.4 Ammonium Hydroxide

As expected at the outset the ammonia model proved to be less accurate than the peroxide. This occurs mainly because of two reasons. Firstly ammonia is a very volatile substance and secondly the titration method used is a back titration, which further increases the error.

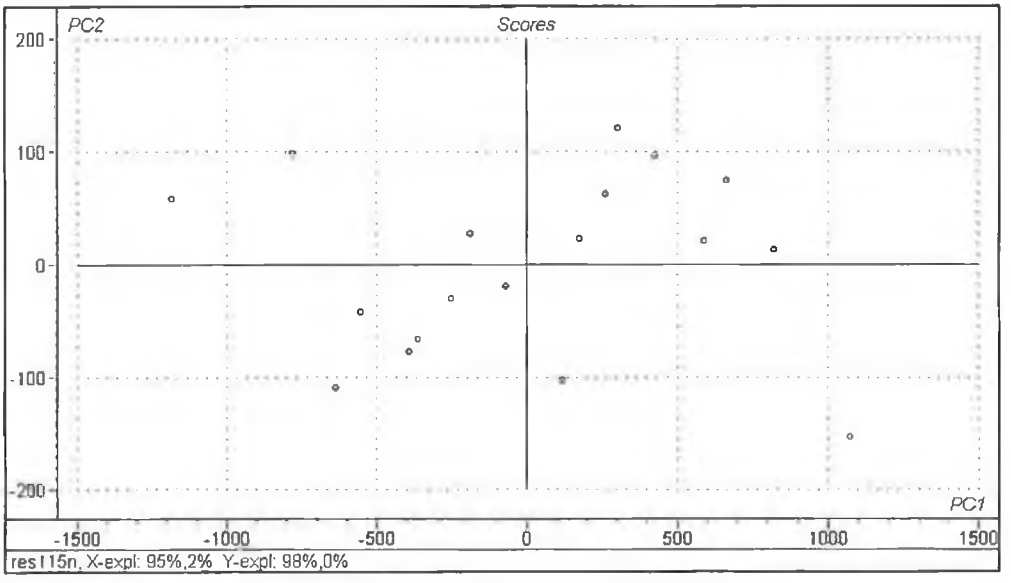

Fig 4-12: Scores plot for NH_4OH molar model.

NH_4OH (mol)	Calibration	Validation	Test-Set	Predicted	Deviation	RMSEP = 0.030
0.334	0.338	0.338	0.181	0.376	0.195	
0.425	0.450	0.451	0.246	0.412	0.166	
0.549	0.501	0.498	0.358	0.527	0.169	
0.591	0.562	0.558	0.374	0.568	0.194	
0.631	0.646	0.647	0.445	0.665	0.220	
0.799	0.793	0.785	0.572	0.773	0.201	

Table 4-4: Calibration and Prediction summary for NH_4OH molar model.

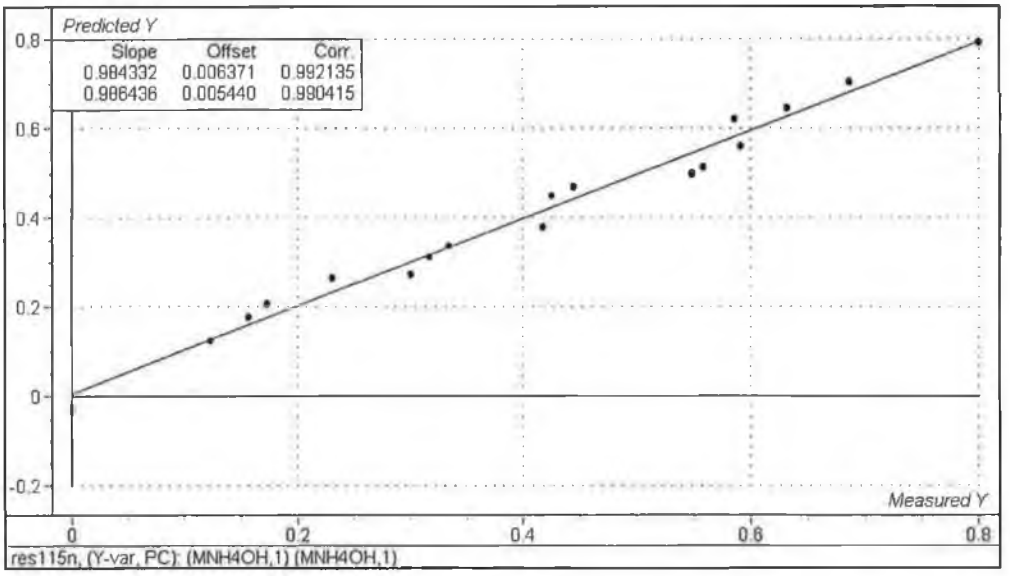

Fig 4-13: Predicted versus Measured Plot for NH_4OH molar model.

The deviations between predicted and titrated values for ammonia as illustrated in Table 4-4 are inordinately large. This is, as discussed in chapter 4, thought to due to the fact that a primary standard was not used in the titrations, but instead NaOH. The problem here is that NaOH absorbs CO_2 from the atmosphere, and does not remain in a pure state over long periods of time. Therefore the problem was in the titrations and *not* in the calibration. Thus a good calibration model was built and could predict percentage values, but was unable to predict molar concentrations, as the NaOH was too unstable. For example as the NaOH degrades over time it takes more of it to react with the excess acid, thus indicating less NH_4OH is present (as it is a back titration, c.f. section 2.6.2).

The calibration and validation values are in line with the titrated values and the RMSEP is reasonably low at 0.03 moles. The test-set, however, predicts values that are in some cases twice as large as predicted values. The fact the predicted values compare very favourably with calibration samples leads one to believe that the NaOH used in the titrations was the source of the problem. A marked

improvement can be seen when a primary standard (Na_2CO_3) is used as in Calibration 2. The NH_4OH molar model thus proved unreliable for prediction purposes. This serves as a useful lesson in that just because a model provides a low RMSEP it does not necessarily mean that it is capable of accurate predictions of unknown test samples.

4.3.3 Calibration 2

A second calibration was performed in an attempt to rectify the NH_4OH molar calibration problem and also to further increase the accuracy of both 'percentage' and molar models

4.3.3.1 Percentage Models, Hydrogen Peroxide

While essentially this calibration set was run to improve the ammonium hydroxide molar model the percentage models are also included in order to illustrate the reproducibility of the technique. Furthermore the errors in this calibration set are again reduced to Calibration 1.

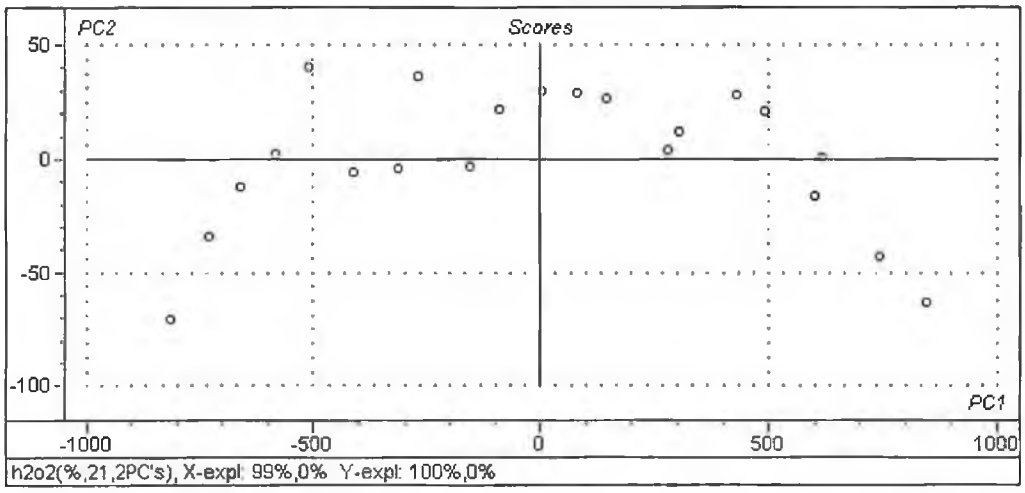

Fig 4-14: Scores plot for H_2O_2 percentage model.

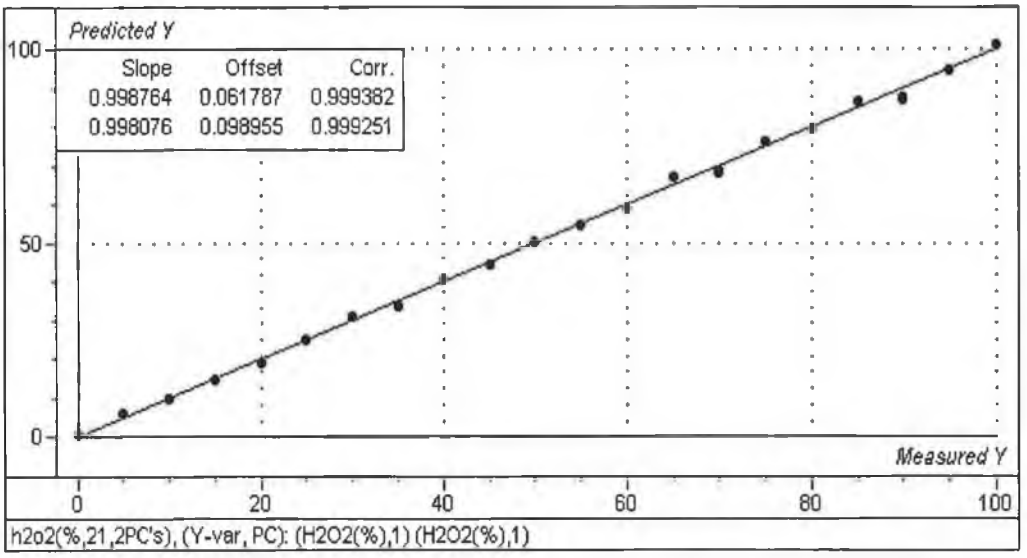

Fig 4-15: Predicted versus Measured Plot for H_2O_2 percentage model.

% H_2O_2	Calibration	Validation	Test-Set	Deviation	RMSEP = 1.17
50	50.15	50.16	50.87	0.87	
60	58.88	58.81	58.19	1.81	
70	68.52	68.41	69.05	0.95	
80	79.72	79.68	78.39	2.61	
90	87.42	87.05	89.22	1.78	
95	94.93	94.87	93.78	1.22	

Table 4-5: Calibration and prediction data summary for second H_2O_2 'percentage' model.

The H_2O_2 calibration set makes an interesting comparison with the H_2O_2 results in 'Calibration 1.' The calibration and validation values are excellent with an error of <2% in all cases bar one, i.e. the 80 % calibration point. The RMSEP, 1.17%, is less than half that in 'Calibration 1' where it is 2.72%. The test set too provides excellent results and this provides proof that this model will predict extremely accurately. The deviations from the expected values for all test solutions are all <2%, which is excellent.

4.3.3.2 Ammonium Hydroxide

Again the main purpose of this model was to compare it with the calibration set in 'Calibration 1' However a second 'percentage' calibration was carried out in an attempt to further reduce prediction errors.

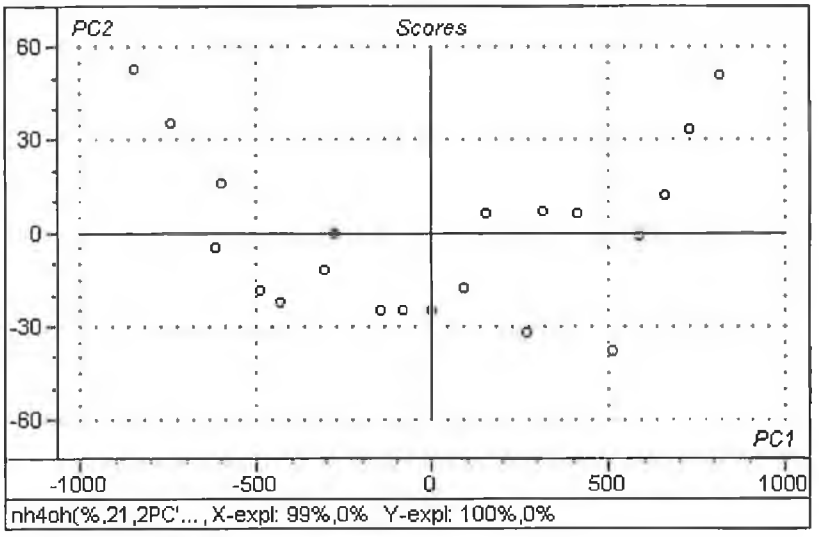

Fig 4-16: Scores Plot for NH_4OH percentage model.

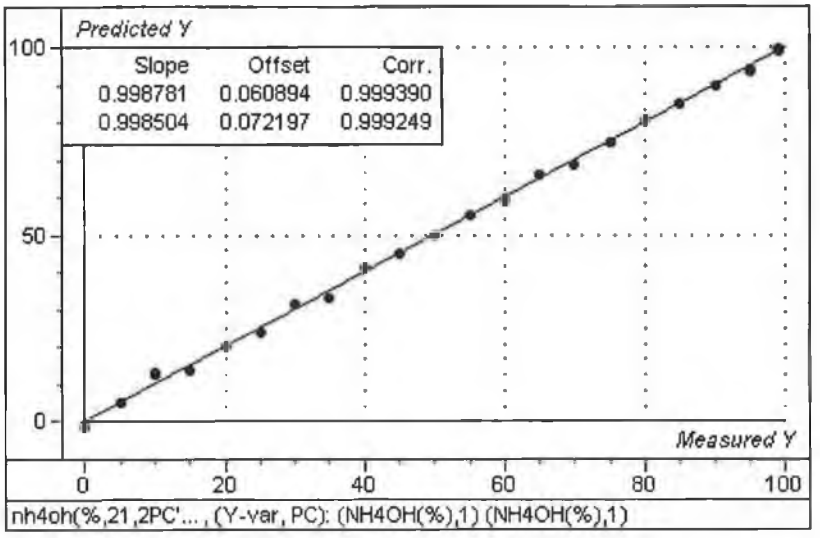

Fig 4-17: Predicted versus measured plot for NH_4OH molar model.

% H_2O_2	Calibration	Validation	Test-Set	Deviation	RMSEP = 1.17
50	49.80	49.79	48.84	1.16	
60	59.33	59.29	58.15	1.85	
70	68.98	68.89	68.55	1.45	
80	80.72	80.76	79.01	0.99	
90	89.89	89.85	88.24	1.76	
95	93.98	93.76	93.47	1.53	

Table 4.6: Calibration and prediction data summary for second NH_4OH 'percentage' model.

The calibration and validation values are very accurate, with a reduction of the RMSEP from 2.72 in Calibration 1 to 1.17 in Calibration 2. The test set again is not as accurate as H_2O_2 for the reasons explained above. However the deviations of the predicted values are reduced from Calibration 1 with the maximum error <2%. This model will predict very accurately NH_4OH percentage with the method described in chapter 2.

4.3.3.3 Molar Models, Hydrogen Peroxide

The main aim of building the new molar models was to provide accurate predictions of the absolute values of NH_4OH. In Calibration 1 this proved impossible due to the unreliability of one of the titrating reagents, NaOH. As discussed earlier this is not a primary standard and therefore experiences changes in concentration over time. This was replaced by sodium carbonate solution (Na_2CO_3) and this allowed for accurate prediction of NH_4OH. This part of the experiment was not confined to NH_4OH as a H_2O_2 model was built, again for comparison purposes and also to reduce prediction errors.

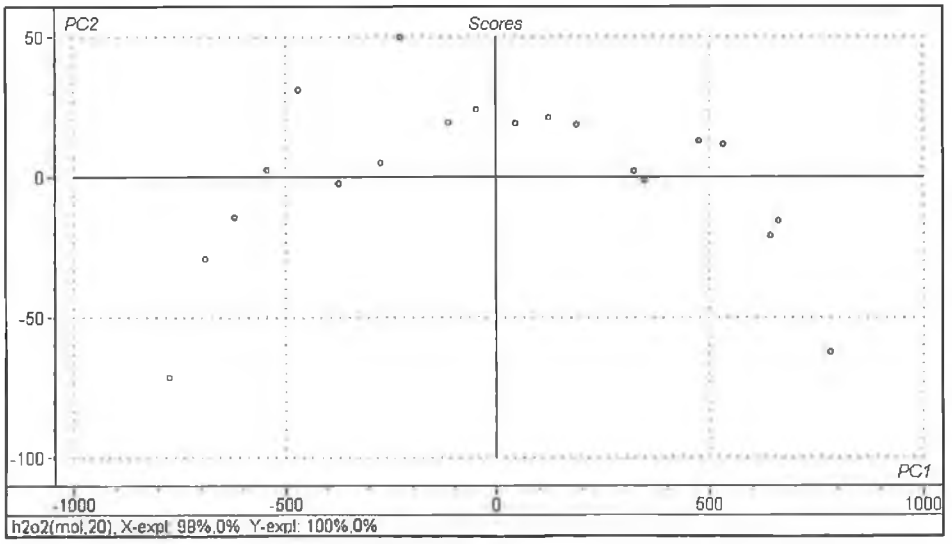

Fig 4-18: Scores plot for H_2O_2 molar model.

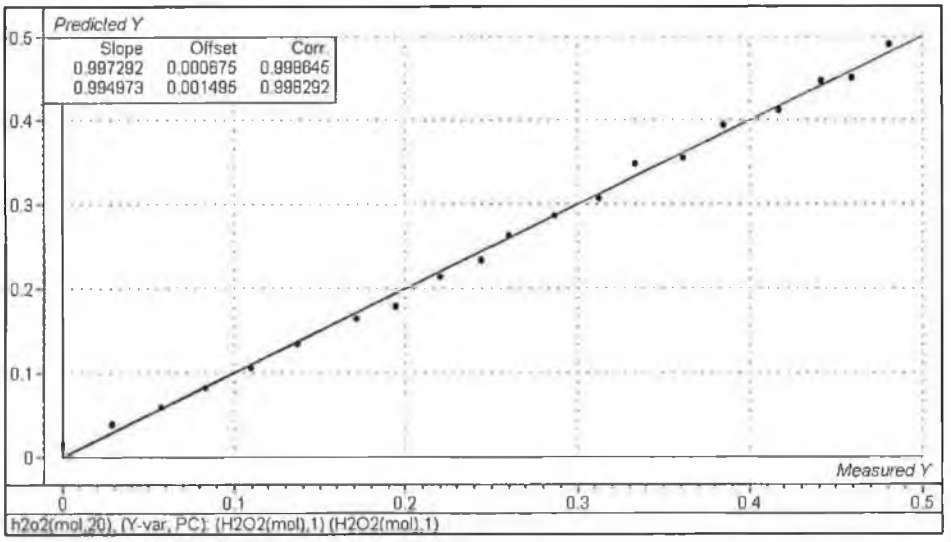

Fig 4-19: Predicted versus plot for H_2O_2 molar model.

H_2O_2 (mol)	Calibration	Validation	Test-Set	Predicted	Deviation	RMSEP = 0.008
0.260	0.263	0.263	0.263	0.259	0.004	
0.312	0.307	0.307	0.298	0.284	0.014	
0.362	0.356	0.355	0.342	0.351	0.009	
0.417	0.413	0.412	0.398	0.406	0.008	
0.459	0.452	0.450	0.439	0.454	0.015	
0.481	0.489	0.491	0.486	0.478	0.008	

Table 4-7: Calibration and prediction data summary for second H_2O_2 molar model.

As evidenced by Table 4-7 this model proved to be the most accurate. When compared to the Calibration 1, molar model the RMSEP is less than half that of the RMSEP of Calibration 1, i.e. 0.008 compared to 0.019. The deviations of the predicted values from the test-set are also less than half that of Calibration 1, reducing to as low as 0.004 in one case.

4.3.3.4 Ammonium Hydroxide

In Calibration 1 it was impossible to predict absolute numbers of moles for NH_4OH. Here it is shown that with a change in the titration method this is, in fact, possible. The Na_2CO_3 remains stable over long periods of time and is a reliable titrant.

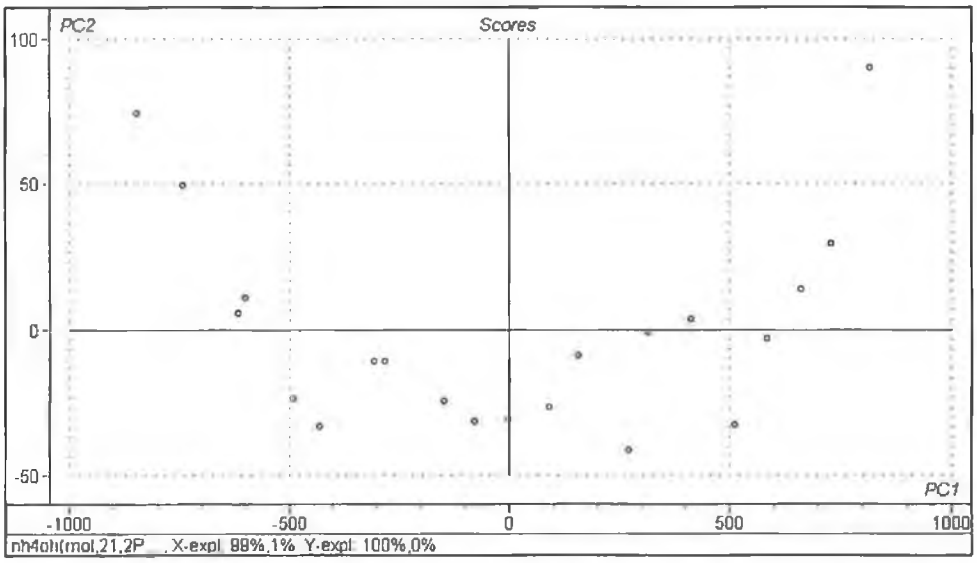

Fig 4-20: Scores Plot for NH_4OH molar model.

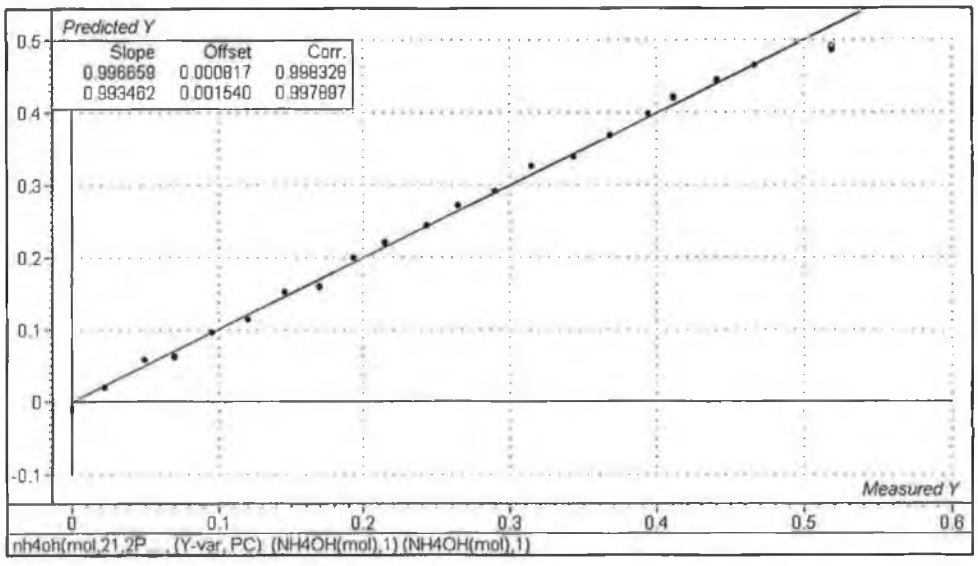

Fig 4-21: Predicted versus plot for NH_4OH molar model.

NH_4OH (mol)	Calibration	Validation	Test-Set	Predicted	Deviation	RMSEP = 0.009
0.243	0.244	0.244	0.238	0.249	0.011	
0.290	0.291	0.291	0.274	0.292	0.018	
0.343	0.339	0.339	0.325	0.342	0.017	
0.394	0.398	0.398	0.386	0.395	0.009	
0.441	0.444	0.444	0.432	0.449	0.017	
0.519	0.491	0.485	0.483	0.498	0.015	

Table 4-8: Calibration and prediction data summary for second NH_4OH molar model.

The results here are comparable with the H_2O_2 model. The RMSEP here is 0.009 moles compared to 0.008 moles in the case of H_2O_2. However it is in the test set that the model proves itself. It is capable of predicting absolute numbers of moles of NH_4OH with deviations of < 0.002 moles, as shown above.

4.3.4 Water Calibration

The water calibration proved more difficult than expected. It was hoped that a water model could be built so that in conjunction with H_2O_2 and NH_4OH the three components of SC-1 could be predicted. However the water variation proved to be

non-linear as shown below and a 4th order polynomial fits to it. PLS cannot deal with non-linear functions and for this reason it was impossible to predict the water concentration using PLS.

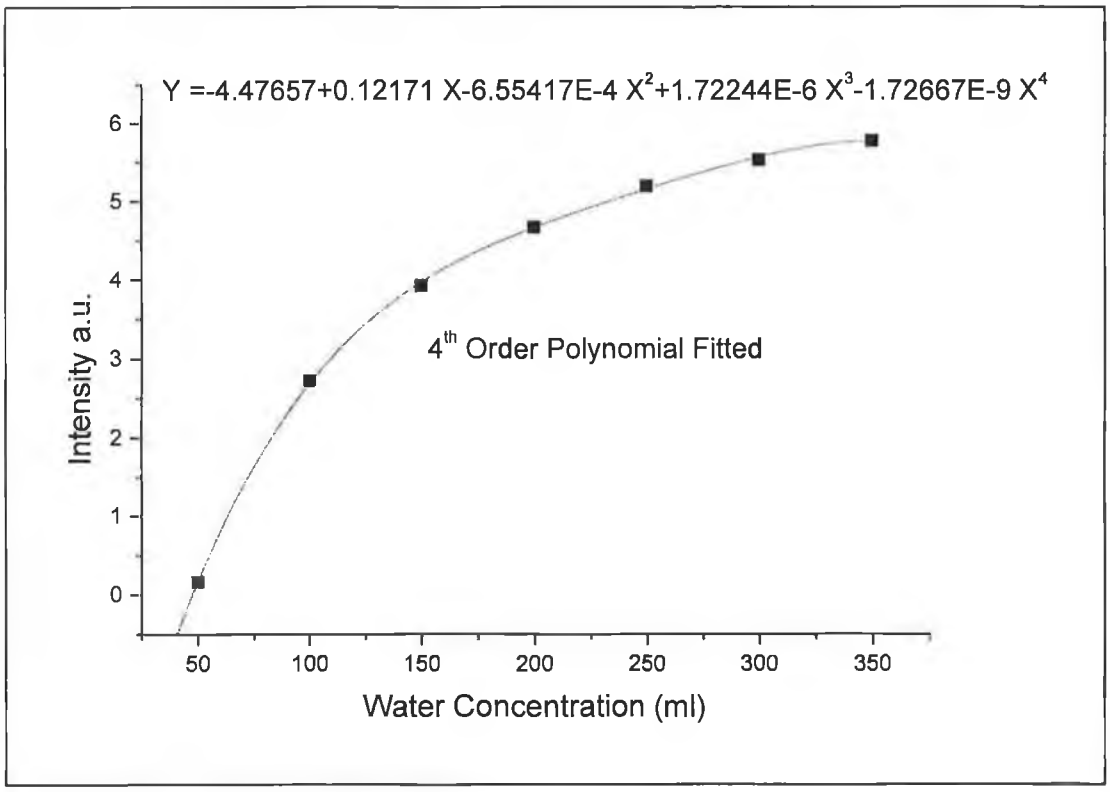

Fig 4-22: Predicted versus Measured plot for water calibration model.

4.4 Conclusion

This chapter has taken us through the various stages involved in building robust calibration and prediction models for the analysis of SC-1 solution. Firstly a univariate analysis was carried out to prove the viability of the approach. The peak areas on the Raman spectra of both H_2O_2 and NH_4OH proved to vary linearly with a change in concentration. From here the multivariate models were built. Firstly a 'percentage' model in order to predict the ratios of H_2O_2 to NH_4OH in a certain solution. Secondly, molar models provided us with predictions of absolute

concentrations. The two multivariate calibrations, including 'percentage' and molar models for both of the reagents in SC-1, proved successful except for the NH_4OH molar model in Calibration 1 for reasons outlined in section 4.3.2.4. This problem was corrected in Calibration 2 and errors were further reduced from Calibration 1.

Chapter 5

Discussion and Conclusions

The aim of this project was to illustrate how Raman spectroscopy combined with various chemometrics techniques could provide a useful tool for process control. SC-1 monitoring has become paramount in the semiconductor industry as both of its main components, hydrogen peroxide (H_2O_2) and ammonium hydroxide (NH_4OH), degrade and evaporate over time leading to non-uniform processing.

The process control application in question, SC-1 monitoring, is suited to Raman spectroscopy because of its well-defined spectral peaks. Both H_2O_2 and NH_4OH produce strong Raman signals at $875cm^{-1}$(O-O stretching vibration) and $3315cm^{-1}$(-NH stretch) respectively. Therefore it was possible to measure peak areas manually for the univariate approach and for the chemometrics package to clearly identify the pertinent peaks. In addition to this, Raman signals vary linearly with a variation in concentration. Therefore, in theory and in practice Raman spectroscopy was an ideal choice for this application.

Chemometrics has quickly become an invaluable tool for process scientists as it enables one to build calibration models and thus predict unknowns from these models. In the SC-1 application chemometrics techniques such as partial least squares regression (PLSR) helps in building both accurate models and allows for quick predictions of unknowns.

The principle in question in this project, i.e. is it possible to predict the concentrations of the individual components of the SC-1 solution spectroscopically, with the possible exception of water was proved with both univariate and

multivariate methods with prediction errors as low as 1.17% for both. The univariate method, however, has no real industrial application, as it proves less accurate than multivariate methods. This is because multivariate methods take every data point into account when building models whereas univariate uses only selected regions of the spectra. However, it does provide the basis for multivariate analysis and is a useful indicator of the possibilities for different applications. In this case it illustrated how the peak area varied linearly with concentration.

Multivariate models, however, prove significantly more powerful than univariate as they take every data point into account. They also predict more accurately and more easily than univariate and it is in such methods as PLSR and PCA that the real industrial applications can be seen, as in this case. Chemometrics, though, is a tool that should be used carefully as it will build models no matter what is entered. Careful consideration should always be given to the variables used and to errors in particular. However a model is robust only if independent test sets can be predicted accurately and also verified. This was the reasoning behind the molar models as the concentrations predicted could be verified independently of the calibration model

The presented models show that chemometrics works best with ratios and to make this project transferable it is imperative that calibrations and predictions are made on the basis of solution ratios and not absolute volumes. However it was a valuable exercise to calibrate and predict absolute numbers to enable to independently verify the concentrations of the components. However it should be noted that there is danger in working with absolute concentrations as can be seen from problems encountered with the initial NH_4OH molar model. Ratios provide a simpler, more effective method that ultimately proves more accurate.

A vital component in this project that proved impossible to predict was the water concentration. Water as seen in chapter 5 produces a non-linear function and this precluded PLS from both calibrating and predicting it properly. A 4^{th} order polynomial was fitted to the data. However it is likely that it is possible to predict it using a univariate analysis technique.

In principle it has been shown that unknown H_2O_2 and NH_4OH concentrations can be predicted from calibration models, in the form of both ratios and absolute concentrations. This could prove invaluable to the semiconductor industry in terms of uniform processing of wafers, productivity enhancement and cost reduction. The models illustrated in chapter 4 show excellent accuracy, with prediction errors of <3% in most cases, and point to the industrial relevance of this project. Allied to this is the fact that it is a non-invasive technique. Yet, the question remains whether or not this technique will be transferable to industry. Further investigations need to be done to incorporate the water concentration into the models to make this a fully viable industrial application.

Bibliography

[1] Kern, W. and Puotinen, D.A., RCA Review, **31,** pp. 187 (1970).

[2] Kern, J. Electrochem. Soc., **137**, 1887 (1990).

[3] Pelletier, M.J., Davis, K. L., Carpio, R.A., Meyappan, M., Economou, D.J., Butler, S.W., Proceedings of the Symposium on Process Control, Diagnostics and Modelling in Semiconductor Manufacturing I. Electrochem. Soc., pp. 282-293 (1995).

[4] Verhaverbeke, S., Parker, J.W., McConnell, C.F., Proceedings of Materials Research Society Symposium. **447**, p47 (1997).

[5] A.A., Gale, G.W., Kashoush, I.I., Precision Cleaning, **II**, p.13 (1994).

[6] Putterman, S.J. Scientific American, p.46 (Feb 1995).

[7] Zhang, D., Kittleson, D.B., Liu, B., Microcontamination Conf. Procceedings, San Jose, CA. p.215 (1994).

[8] Itano, M., Kern Jr, F.W., Rosenberg, R.W., Miyashita, M., Kawanabe, I., Ohmi, T., IEEE Transactions on Seimconductor Manufacturing, **5**, p.114 (1992).

[9] Kobayshi, H., Ryuta, J., Shingyuji, Shimanuki, Y., Jpn. J. Appl. Phys., **32**, pp. L45-47, Part 2, No. 1A/B (1993).

[10] Meuris, M., Verhaverbeke, S., Mertens, P.W., Heyns, M.M., Hellemans, L. Bruynseraede and Philipossian, A., Jpn. J. Appl. Phys., **31**, pp. L1514-1517, Part 2, No. 11A (1992).

[11] Kaigawa, H., Yamamoto, K., Shigematsu, Y., Jpn. J. Appl. Phys., **33** pp. 4080-4085, Part 1, No. 7A, (1994).

[12] Kern, W., Semicond. Int., p.94 (1984).

[13] van den Meerakker, J.E.A.M., van der Stratten, M.Y.M., J. Electrochem. Soc., **137**, p.1239(1990).

[14] Tanaka, K., Sakurai, S., Kamizuma, S., Shimanuki, Y., J. Electrochem. Soc. Ext. Abstr., p.689 (1990).

[15] Tanaka, K., Sakurai, S., Kamizuma, S., Shimanuki, Y., J. Electrochem. Soc. Ext. Abstr., p.710 (1990).

[16] Sugihara, Y., Shimokawa, S., Oshida, Y., Chemical Proceedings of the Semiconductor Pure Water and Chemicals Conference, M.J. Balzas, Editr, Balzas Analytical Laboratory (1993).

[17] Takahashi, I., Kobayshi, H., Ryuta, J., Kishimoto, M., Shingyouji, T., Jpn. J. Appl. Phys., **32**, pp. L1183-L1185, Part 2, No. 9A, (1993).

[18] Carpio, R., Soucy, J., Peterman, S., Jahanbani, M., Electrochem. Soc. Proc. **III**, Contamination Control and Defect Reduction in Semiconductor Manufacturing , (1994).

[19] Barakaev, A.K., Glushkov, S.M., Panchishin, I.M., Zhurnal Prikladnoi Spektroskopii, **55**, p.375 (1991).

[20] Pelletier, M.J., Davis, K.L., Carpio, R.A., Semiconductor International, pp. 103-108 (March 1996).

[21] CS-200 product literature from Horiba Instruments Incorporated, Kyolo, Japan

[22] D.S. Knight and W.B. White, J. Mater. Res., **4(2),** pp.385-393 (1989).

[23] S. Farquharson and S.F. Simpson, Applications of Raman spectroscopy to industrial processes, SPIE **1681**, pp.276-290 (1992).

[24] A.M. Tudor, M.C. Davies, C.D. Melia, D.C. Lee, R.C. Mitchell, P.J. Hendra and S.J. Church, The applications of near infra-red Fourier transform Raman spectroscopy to the analysis of polymorphic forms of cimetidine, Spectrochim. Acta., **47A**, pp.1389-1393 (1991).

[25] Ingrid De Wolf, Micro Raman spectroscopy to study local mechanical stress in silicon integrated circuits., Semicond. Sci. Technol., **11**, pp.139-154 (1996).

[26] J.B. Cooper, P.E. Flecher, T.M. Vess and W.T. Welch, Remote fibre-optic Raman analysis of xylene isomers in mock petroleum fuels using a low cost dispersive instrument and partial least-square regression analysis, Appl. Spectrosc., **49**, pp.586-592 (1995).

[27] J.B. Cooper, K.L. Wise, J. Groves, and W.T. Welch, Determination of octane numbers and Reid vapour pressure of commercial petroleum fuels using FT-Raman spectroscopy and partial least-squares regression analysis, Anal. Chem., **67**, pp.4096-4100 (1995).

[28] Smekal, A., Naturwiss., **11**, p.873 (1923).

[29] *Practical Raman Spectroscopy*, Gardiner, D.J., Graves, P.R., Springer-Verlag Berlin Heidelberg, (1989).

[30] Behringer, J., The Relation of Resonance Raman Scattering to resonance Fluouescence, Journal of Raman Spectroscopy, **2(3)**, pp.275-299 (1974).

[31] Molecular Spectroscopy, **2**, The Chemical Society, London (1974).

[32] Baranska, H., Kabudzinska, A., Terpinski, J., *Laser Raman Spectrometry, Analytical Applications*, Ellis Horwod Limited, (1987).

[33] Raman, C.V., Nature, pp. 121, 501, 619, 721, (1928).

[34] Tedesco, J.M.; Owen H., Pallister, D.M., Morris, M.D., Anal. Chem. **65**, p.441A (1993).

[35] Massart, D.L., Vandeginste, B.G.M., Dening, S.M., Michotte, Y., Kaufman L., *Chemometrics: a textbook*

[36] Martens, H., Naes T., Multivariate Calibration, Wiley 1989.

[37] Chemometrics for Beginners, *Near Infra-Red Publications* (NIRP) Training (May 1998).

Apppendix A

PCA Algorithm[36]

The algorithm extracts one factor at a time. Each factor is obtained iteratively by repeated regressions of X on scores $\hat{t}$ to obtain improved $\hat{p}$, and of X on these $\hat{p}$ to obtain improved $\hat{t}$. The algorithm proceeds as follows:

Pre-scale the X-variables to ensure comparable noise levels. Then centre the X-variables, e.g. by subtracting the calibration means $\bar{x}'$, forming X_0. Then for factors $a = 1,2,...,A$ compute $\hat{t}_a$ and $\hat{p}_a$ from X_{a-1}:

Start:

Select start values, e.g. $\hat{t}_a$ = the column in X_{a-1} that has the highest remaining sum of squares.

Repeat points i) to v) until convergence.

i) Improve estimate of loading vector $\hat{p}_a$ for this factor by projecting the matrix X_{a-1} on $\hat{t}_a$, i.e.

$$\hat{p}_a' = \left(\hat{t}_a'\hat{t}_a\right)^{-1}\hat{t}_a'X_{a-1}$$

ii) Scale length of $\hat{p}_a$ to 1.0 to avoid scaling ambiguity:

$$\hat{p}_a = \hat{p}_a\left(\hat{p}_a'\hat{p}_a\right)^{-0.5}$$

iii) Improve estimate of score $\hat{t}_a$ for this factor by projecting the matrix X_{a-1} on $\hat{p}_a$:

$$\hat{t}_a = X_{a-1}\hat{p}_a\left(\hat{p}_a'\hat{p}_a\right)^{-1}$$

iv) Improve the estimate of the eigenvalue $\hat{\tau}_a$:

$$\hat{\tau}_a = \hat{t}_a' \hat{t}_a$$

v) Check convergence: If $\hat{\tau}_a$ minus $\hat{\tau}_a$ in the previous iteration is smaller than a certain small pre-specified constant, e.g. 0.0001 times $\hat{\tau}_a$, the method has converged for this factor. If not go to step i).

$$\mathrm{X}_a = \mathrm{X}_{a-1} - \hat{\tau}_a \hat{p}_a'$$

and go to *Start* for the next factor.

Appendix B

PLS1 Algorithm[36]

Calibration:

C1 The scaled input variables X and y are first centered, e.g.

$$\mathrm{X}_0 = \mathrm{X} - 1\bar{x}' \text{ and } y_0 = y - 1\bar{y}.$$

Choose A_{max} to be higher than the number of phenomena expected in X.

For each factor a=1,….,A_{max} perform steps 2.1-2.5:

C 2.1 Use the variability remaining in y to find the loading weights w_a, using least squares and the local 'model'.

$$\mathrm{X}_{a-1} = y_{a-1} w_a' + E$$

and scale the vector to length 1. The solution is

$$\hat{w}_a = cX'_{a-1} y_{a-1}$$

where c is the scaling factor that makes the length of the final $\hat{w}_a$ equal to 1, i.e.

$$c = (y'_{a-1} X_{a-1} X'_{a-1} y_{a-1})^{0.5}$$

C 2.2 Estimate the scores $\hat{t}_a$ using the local 'model'

$$X_{a-1} = t_a \hat{w}'_a + E$$

The LS solution is (since $\hat{w}_a' \hat{w}_a = 1$)

$$\hat{t}_a = X_{a-1} \hat{w}_a$$

C 2.3 Estimate the spectral loadings p_a using the local 'model'

$$X_{a-1} = t_a p_a' + E$$

which gives the LS solution

$$\hat{p}_a = X_{a-1}' \hat{t}_a / \hat{t}_a' \hat{t}_a$$

Estimate the chemical loading q_a using the local 'model'

$$y_{a-1} = \hat{t}_a q_a + f$$

which gives the solution

$$\hat{q}_a = y_{a-1}' \hat{t}_a / \hat{t}_a' \hat{t}_a$$

C 2.5 Create new X and y residuals by subtracting the estimated effect of this factor:

$$\hat{E} = X_{a-1} - t_a p_a'$$

$$\hat{f} = y_{a-1} - \hat{t}_a q_a$$

Compute various summary statistics on these residuals after a factors, summarising $\hat{e}_{ik}$ over objects i and variables k, and summarising $\hat{f}_i$ over i objects. Replace the former X_{a-1} and y_{a-1} by the new residuals $\hat{E}$ and $\hat{f}$

$$X_a = \hat{E}$$

$$y_a = \hat{f}$$

$$a = a+1$$

C 3 Determine A, the number of valid PLS factors to retain in the calibration model.

C 4 Compute $\hat{b}_0$ and $\hat{b}$ for A PLS factors, to be used in the predictor

$$\hat{y} = 1\hat{b}_0 + X\hat{b}$$

$$\hat{b} = \hat{W}(\hat{P}'\hat{W})^{-1}\hat{q}$$

$$\hat{b}_0 = \bar{y} - \bar{x}'\hat{b}$$

Prediction:

Full Prediction

For each new prediction object i = 1,2,….perform steps P1 to P3, or alternatively, step P4.

P 1 Scale input data x_i like as for the calibration variables. Then compute

$$x'_{i,0} = x'_i - \bar{x}'$$

where $\bar{x}$ is the centre for the calibration objects.

For each factor a = 1,…., A perform steps P 2.1-P2.2.

P 2.1 Find $\hat{t}_{i,a}$ according to the formula in C 2.2 i.e.

$$\hat{t}_{i,a} = x'_{i,a} - 1\hat{w}_a$$

P 2.2 Compute new residual $x_{i,a} = x_{i,a-1} - \hat{t}_{ia}\hat{p}'_a$

If $a < A$, increase a by 1 and go to P 2.1. If $a = A$, go to P 3.

P 3 Predict y_i by $\hat{y}_i = \bar{y} + \sum_{a=1}^{A} \hat{t}_{i,a}\hat{q}$

Compute outlier statistics on $x_{i,A}$ and $\hat{t}_i$

Short Prediction

P 4 Alternatively to steps P 1 – P 3, find $\hat{y}$ by using $\hat{b}_0$ and $\hat{b}$ in C 4, i.e.

$$\hat{y} = \hat{b}_0 + x_i'\hat{b}$$